

Efficient Coding by Midget and Parasol Ganglion Cells in the Human Retina

Highlights

- Large-scale recordings of midget and parasol ganglion cells in the human retina
- Receptive fields of midget and parasol ganglion cells cover frequency space jointly
- Response functions of ON and OFF types intersect at negative contrast
- Receptive fields and response functions support efficient coding of natural stimuli

Authors

Florentina Soto, Jen-Chun Hsiang, Rithwick Rajagopal, ..., Philip Custer, Josh L. Morgan, Daniel Kerschensteiner

Correspondence

kerschensteinerd@wustl.edu

In Brief

Soto et al. combine large-scale multi-electrode array recordings of human retinas and computational modeling to show that ON and OFF midget and ON and OFF parasol ganglion cells efficiently encode luminance contrast in our environment.

Report

Efficient Coding by Midget and Parasol Ganglion Cells in the Human Retina

Florentina Soto,^{1,6} Jen-Chun Hsiang,^{1,2,6} Rithwick Rajagopal,¹ Kisha Piggott,¹ George J. Harocopos,¹ Steven M. Couch,¹ Philip Custer,¹ Josh L. Morgan,¹ and Daniel Kerschensteiner^{1,3,4,5,7,*}

¹John F. Hardesty, MD, Department of Ophthalmology and Visual Sciences, Washington University School of Medicine, Saint Louis, MO 63110, USA

²Graduate Program in Neuroscience, Washington University School of Medicine, Saint Louis, MO 63110, USA

³Department of Neuroscience, Washington University School of Medicine, Saint Louis, MO 63110, USA

⁴Department of Biomedical Engineering, Washington University School of Medicine, Saint Louis, MO 63110, USA

⁵Hope Center for Neurological Disorders, Washington University School of Medicine, Saint Louis, MO 63110, USA

⁶These authors contributed equally

⁷Lead Contact

*Correspondence: kerschensteinerd@wustl.edu

<https://doi.org/10.1016/j.neuron.2020.05.030>

SUMMARY

In humans, midget and parasol ganglion cells account for most of the input from the eyes to the brain. Yet, how they encode visual information is unknown. Here, we perform large-scale multi-electrode array recordings from retinas of treatment-naïve patients who underwent enucleation surgery for choroidal malignant melanomas. We identify robust differences in the function of midget and parasol ganglion cells, consistent asymmetries between their ON and OFF types (that signal light increments and decrements, respectively) and divergence in the function of human versus non-human primate retinas. Our computational analyses reveal that the receptive fields of human midget and parasol ganglion cells divide naturalistic movies into adjacent spatiotemporal frequency domains with equal stimulus power, while the asymmetric response functions of their ON and OFF types simultaneously maximize stimulus coverage and information transmission and minimize metabolic cost. Thus, midget and parasol ganglion cells in the human retina efficiently encode our visual environment.

INTRODUCTION

How nervous systems transform signals from the environment into internal representations is a central question of neuroscience. In humans, we have unique access to internal representations and rich psychophysical data on their relationship to sensory stimuli (Kingdom and Prins, 2016), but we lack insights into the underlying neuronal signal transformations (Weinstein et al., 1971).

Vision begins in the retina, which extracts information from the influx of photons to the eye and sends it to the brain via the spike trains of ganglion cells. Midget and parasol ganglion cells account for ~80% of the input from the eye to the brain in humans and non-human primates (Dacey, 1993, 2004; Dacey and Peteresen, 1992; Field and Chichilnisky, 2007; Masri et al., 2019a). The light responses of midget and parasol ganglion cells have been studied extensively in macaques (Dacey, 2004; Field and Chichilnisky, 2007; Grimes et al., 2018) but remain unknown in humans. Approximately 25 million years of independent evolution separate humans and macaques (Disotell and Tosi, 2007); for scale, the ancestors of humans and mice diverged ~87 million years ago (Springer et al., 2003). Furthermore, although

psychophysical studies found broad overlap in the visual performance of humans and non-human primates, they also noted significant differences, including in low-level functions like contrast sensitivity (Matsuno and Fujita, 2009; Sasaoka et al., 2005). Therefore, to evaluate evolutionary divergence in function and understand how we see the world, we need to study midget and parasol ganglion cells in the human retina.

Spatiotemporal variations in brightness (i.e., luminance contrast) drive neuronal responses throughout the early visual system and shape our perception of the world (Delorme et al., 2000; Kaplan, 2008; Nassi and Callaway, 2009; Stone et al., 1990). At the first synapse of the visual system, luminance contrast is split into parallel pathways that signal light increments (ON) and decrements (OFF), respectively (Euler et al., 2014). Several ganglion cells, including midget and parasol, have matching ON and OFF types, referred to as paramorphic pairs (Dacey, 2004; Famiglietti, 2004; Masri et al., 2019b). Indeed, paired ON and OFF channels are a common feature of many sensory systems (Chalasanani et al., 2007; Gallio et al., 2011; Joesch et al., 2010; Saha et al., 2013; Saunders and Bastian, 1984; Scholl et al., 2010), indicating that they represent an optimal solution to a shared problem (Gjorgjieva et al., 2014, 2019).

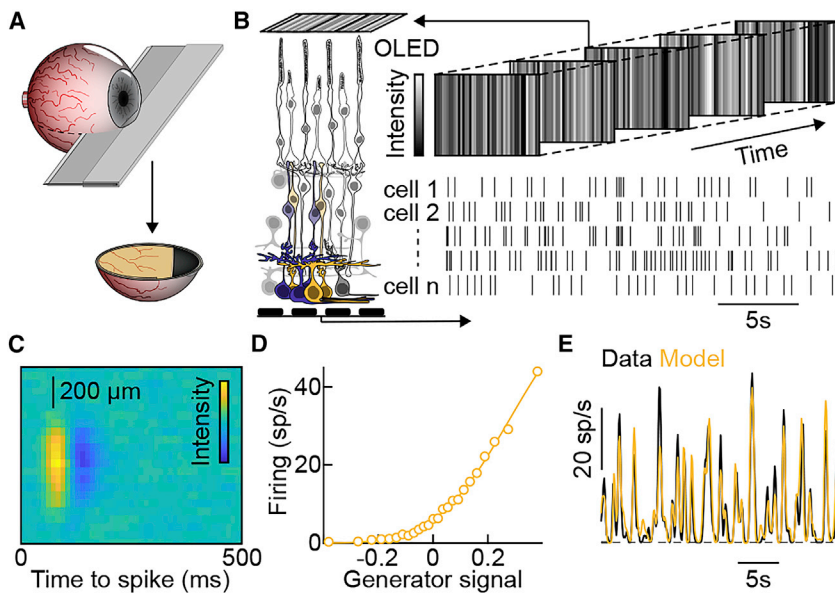


Figure 1. Multi-electrode Array Recordings of the Human Retina

(A) In the operating room, enucleated eyes were dissected front to back on the non-tumor side of the optic nerve under transillumination. Care was taken not to detach the retina from the underlying pigment epithelium.

(B) Ganglion cell responses to a spatiotemporal white-noise stimulus were recorded on planar multi-electrode arrays.

(C) Spatiotemporal receptive field map of a representative ganglion cell measured as the spike-triggered stimulus average during one segment of the white noise presentation.

(D) The nonlinear relationship between the firing rate of the same cell and the match between the receptive field and stimulus (i.e., the generator signal or effective contrast) measured during a second segment of the recording.

(E) Overlay of the linear-nonlinear (LN) model (C and D) predictions of the cell and its responses during a third segment of the recording. The LN model predicted 79% of the variance in the response of this cell (mean \pm SEM variance explained across all cells analyzed: 64% \pm 1%)

See also [Figure S1](#).

However, whether and how paramorphic midget and parasol ganglion cells are optimized to encode luminance contrast in our environment remains obscure.

The optic nerve is a bottleneck for the transmission of visual information. Its diameter limits the number of ganglion cells sending signals to the brain, and its length contributes to the metabolic cost of action potentials conveying these signals (Ju et al., 2016; Meister, 2003). Efficient coding theory predicts that under such constraints, neurons should encode visual scenes efficiently by limiting the redundancy between cells and the firing rate of each (Attneave, 1954; Barlow, 1961; Pitkow and Meister, 2012). How the response properties of human midget and parasol ganglion cells align with the statistics of our natural environment and whether this alignment matches predictions of efficient coding theory is unclear.

Here, we perform large-scale multi-electrode array recordings from human retinas to characterize luminance contrast responses of ON and OFF midget and ON and OFF parasol ganglion cells and use computational modeling to analyze information encoding of these cells in our natural environment.

RESULTS

We obtained retinas from four treatment-naive patients with (near-)normal vision (best corrected visual acuity: $\geq 20/50$) and normal intraocular pressure (10–15 mm Hg) who underwent enucleation surgery for choroidal malignant melanomas. Eyes were dissected less than 5 min after central artery occlusion, and eyecup preparations from the non-tumor-side of the optic nerve transferred into Ames' medium in an oxygenated chamber and dark-adapted for more than 1 h (Figure 1A). The subsequently isolated retinas exhibited robust light responses, which we recorded on multi-electrode arrays. To probe luminance contrast coding of midget and parasol ganglion cells, we pre-

sented an achromatic spatiotemporal white-noise stimulus (Figure 1B) and analyzed neural responses using a linear-nonlinear (LN) model (Chichilnisky, 2001; Pearson and Kerschensteiner, 2015). We first mapped the spatiotemporal receptive field (i.e., the linear part of the model) of each cell by reverse correlating its spike train to one segment of the stimulus (Figure 1C). We then estimated the dependence of its firing rate on the match between the stimulus and the receptive field (i.e., the nonlinear part of the model) from a second segment of the recording (Figure 1D). This match between stimulus and receptive field, traditionally called the generator signal, can be thought of as the effective stimulus contrast. We, therefore, refer to the nonlinear part of the model as the cell's contrast-response function. Finally, we tested the ability of the LN models to predict spike responses during a third segment of the recording (Figure 1E). Only cells whose LN model explained >35% of their response variance (81% of the recorded cells) were considered light-responsive and retained for further analysis (see STAR Methods).

To identify functional ganglion cell types, we devised a serial classification approach, which separated ON and OFF midget and ON and OFF parasol ganglion cells by their temporal receptive fields (Figure S1; STAR Methods). Importantly, cell types identified in this way exhibited consistent differences in their spatial receptive fields and contrast-response functions, which were not part of the classification, supporting the validity of our approach. The naming of midget and parasol ganglion cells is based on functional similarities to these cell types in non-human primates (Chichilnisky and Kalmr, 2002; Croner and Kaplan, 1995; Sinha et al., 2017) and matches between spatial receptive fields in our study and dendritic fields measured anatomically in human retinas (Dacey, 1993; Dacey and Petersen, 1992; Masri et al., 2019a). Together, midget and parasol ganglion cells accounted for $\sim 80\%$ (336/424) of the light-responsive cells we recorded.

In the fovea, midget ganglion cells receive private-line input from individual cone photoreceptors and mediate high acuity and color vision (Dacey, 2004; Kolb and Marshak, 2003; Sabsan et al., 2016; Sinha et al., 2017; Wässle et al., 1994). In the peripheral retina, midget ganglion cells receive convergent cone input and, in non-human primates, their spatial resolution and color-opponency are reduced (Field et al., 2010; Martin et al., 2001; Sinha et al., 2017; Wool et al., 2018). Our recordings from peripheral human retinas revealed asymmetries in the luminance contrast coding of ON and OFF midget ganglion cells (Figures 2 and S2). Temporal receptive fields of ON cells were narrower and more biphasic than those of OFF cells (Figures 2A, 2B, 2G, and 2H). In contrast, spatial receptive fields of ON cells were broader than those of OFF cells (Figures 2C, 2D, and 2I), consistent with differences in the dendritic fields of these cells (Dacey and Petersen, 1992). Finally, the contrast-response functions of ON midget ganglion cells had lower thresholds, higher gain, and were more linear than those of OFF midget ganglion cells (Figures 2E, 2F, and 2J–2L).

We observed similar ON-OFF asymmetries for parasol ganglion cells (Figures 3 and S3). Thus, the temporal receptive fields of ON cells were more biphasic than those of OFF cells (Figures 3A, 3B, 3G, and 3H) and their spatial receptive fields were larger (Figures 3C, 3D, and 3I), matching anatomical findings (Dacey and Petersen, 1992). The contrast-response functions of ON parasol ganglion cells had lower thresholds, higher gain, and were more linear than those of OFF parasol ganglion cells (Figures 3E, 3F, and 3J–3L). Compared to midget ganglion cells, parasol ganglion cells had narrower and more biphasic temporal receptive fields (Figures 3M and 3N), broader spatial receptive fields (Figure 3O), and lower response thresholds (Figures 3P–3R). These differences between midget and parasol ganglion cells were consistent for ON and OFF types. Neither midget nor parasol ganglion cells were direction selective in their responses to drifting grating stimuli (Figure S4).

Through evolution, sensory systems are shaped by the statistics of the environments in which they operate (Baden et al., 2020; Cronin et al., 2014; Simoncelli, 2003). To understand the observed differences in spatiotemporal receptive fields of ON and OFF midget and ON and OFF parasol ganglion cells in this context, we transformed space-time maps (Figures 2 and 3) into spatial and temporal frequency-domain filters (Figures 4A and 4B). We then analyzed the spatiotemporal frequency composition of movies recorded in different natural environments (Figure 4C), taking into account the nonlinear projection of the human eye and fixational eye movements (see STAR Methods) (Drasdo and Fowler, 1974; Van Der Linde et al., 2009). Placing the neural filters in the resulting landscapes revealed that ON and OFF midget and ON and OFF parasol ganglion cells fall along adjacent sections of a single power line (Figure 4D). This suggests that the receptive fields of these four cell types divide naturalistic movies into adjacent spatiotemporal frequency domains of equal stimulus power.

Following this insight into the organization of spatiotemporal filters (i.e., receptive fields), we next explored the arrangement of the contrast-response functions that transform filtered inputs into spike responses. Previous modeling showed that parsing luminance contrast into paired ON and OFF channels can

reduce the number of spikes and thus the metabolic expenditure needed to encode stimulus distributions (Gjorgjieva et al., 2014, 2019). In both midget and parasol ganglion cells, we observed consistent asymmetries between the contrast-response functions of ON and OFF types (Figures 2 and 3). In particular, contrast thresholds of ON cells were much lower than those of OFF cells, and their response functions were more linear and had higher gain. As a result, rather than splitting contrast encoding down the middle, response functions of paramorphic midget and parasol ganglion cell pairs intersected at negative contrasts. Importantly, this finding derived from LN models held true for responses of ON and OFF midget and ON and OFF parasol cells to full-field contrast steps (Figure S5).

To explore potential reasons for the ON-OFF asymmetries in contrast-response functions, we convolved naturalistic movies with spatiotemporal receptive fields of ON and OFF midget and ON and OFF parasol ganglion cells to reveal effective contrast distributions (Figure 4E). We then moved the intersection of the experimentally determined response functions of paramorphic pairs along the contrast axis, calculating at each point the energy spent per channel and on aggregate (Figure 4F) and the fraction of the stimulus distributions within the dynamic ranges of the response functions (i.e., stimulus coverage, Figure 4G). Energy consumption was minimized and balanced between ON and OFF channels when their response functions intersected at negative contrasts (Figures 4F and 4H). Intriguingly, negative shifts also maximized stimulus coverage (Figures 4G and 4H). Finally, we computed the mutual information between naturalistic movies and predicted spike responses of ON and OFF midget and ON and OFF parasol ganglion cells at different contrast offsets (Figure 4G). Similar to stimulus coverage, mutual information was maximized when response functions of paramorphic pairs, both midget and parasol, intersected at negative contrasts (Figures 4G and 4H).

DISCUSSION

Here, we use large-scale multi-electrode array recordings to analyze the luminance contrast encoding of midget and parasol ganglion cells in the human retina. Consistent with anatomical studies (Dacey, 1993; Dacey and Petersen, 1992; Masri et al., 2019a), ON and OFF midget and ON and OFF parasol ganglion cells accounted for the majority of cells (~80%) in our recordings. Among the remaining cells, we observed ON-OFF and suppressed-by-contrast responses (data not shown), indicating further diversity and potential evolutionary conservation in the less abundant signals from our eyes to our brain (Chichilnisky and Baylor, 1999; Dacey and Lee, 1994; de Monasterio, 1978; Tien et al., 2015).

We find that spatiotemporal receptive fields, which filter visual inputs, differ consistently between midget and parasol ganglion cells and between paramorphic ON and OFF types. The spatial receptive fields of parasol ganglion cells are larger than those of midget ganglion cells, and the spatial receptive fields of ON types are larger than those of OFF types (Figures 2 and 3). In mice, rabbits, and cats, the receptive fields of ganglion cells align with their dendrites (Brown et al., 2000; Peichl and Wässle, 1983;

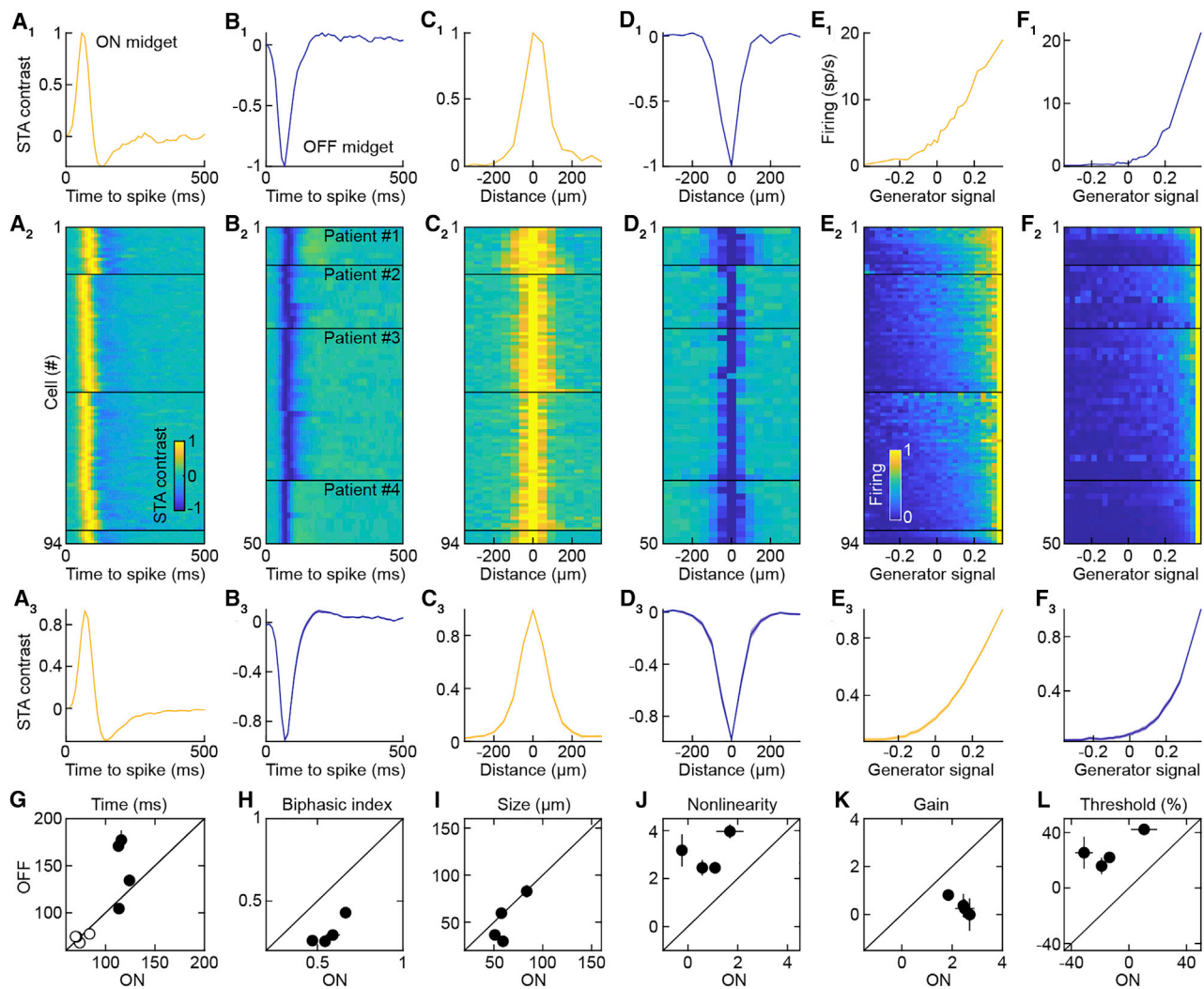


Figure 2. Functional Characterization of ON and OFF Midget Ganglion Cells

(A₃–B₃) Temporal receptive fields of individual ON (A₁) and OFF (B₁) midget ganglion cells, all ON (A₂) and OFF (B₂) midget ganglion cells grouped by patients and sorted by their time to peak, and the average (±SEM) of all ON (A₃) and OFF (B₃) midget ganglion cells.

(C₃–D₃) Spatial receptive fields of individual ON (C₁) and OFF (D₁) midget ganglion cells, all ON (C₂) and OFF (D₂) midget ganglion cells grouped by patients and sorted by their size, and the average (±SEM) of all ON (C₃) and OFF (D₃) midget ganglion cells.

(E₃–F₃) Static nonlinearities (or effective-contrast-response functions) of individual ON (E₁) and OFF (F₁) midget ganglion cells, all ON (E₂) and OFF (F₂) midget ganglion cells grouped by patients and sorted by their threshold, and the average (±SEM) of all ON (E₃) and OFF (F₃) midget ganglion cells.

(G–L) Summary data (mean ± SEM) comparing time to peak (G, TTP all $p > 0.1$, $\eta^2 = 0.08 \pm 0.03$, empty circles), time to zero-crossing (G, TTZ $p < 0.05$ except for patient 4, $\eta^2 = 0.47 \pm 0.14$, filled circles), biphasic index (H, all $p < 0.01$, $\eta^2 = 0.60 \pm 0.06$), receptive field size (I, $p < 0.001$ except for patients 1 and 4, $\eta^2 = 0.28 \pm 0.14$), nonlinearity (J, all $p < 0.01$, $\eta^2 = 0.52 \pm 0.05$), gain (K, all $p < 0.01$, $\eta^2 = 0.40 \pm 0.11$), and threshold (L, all $p < 0.01$, $\eta^2 = 0.49 \pm 0.05$) of ON versus OFF midget ganglion cells.

See also [Figure S2](#).

[Schwartz et al., 2012](#); [Yang and Masland, 1992](#)). The differences we observe in receptive field sizes are consistent with anatomical reconstructions of ON and OFF midget and ON and OFF parasol ganglion cells in the human retina ([Dacey, 1993](#); [Dacey and Petersen, 1992](#); [Masri et al., 2019a](#)). Based on this correlation and previous anatomical results ([Dacey and Petersen, 1992](#)), we expect differences in midget and parasol ganglion cell receptive field sizes to increase toward the fovea.

The temporal receptive fields of parasol ganglion cells in our dataset were faster and more biphasic than those of midget ganglion cells, and the temporal receptive fields of ON types were more biphasic than those of OFF types ([Figures 2 and 3](#)). Temporal receptive fields of ganglion cells are shaped by the kinetics of their excitatory input from bipolar cells ([Awatramani and Slaughter, 2000](#); [Diamond and Copenhagen, 1995](#); [Puthusseray et al., 2014](#); [Sinha et al., 2017](#)). Biphasic receptive fields indicate

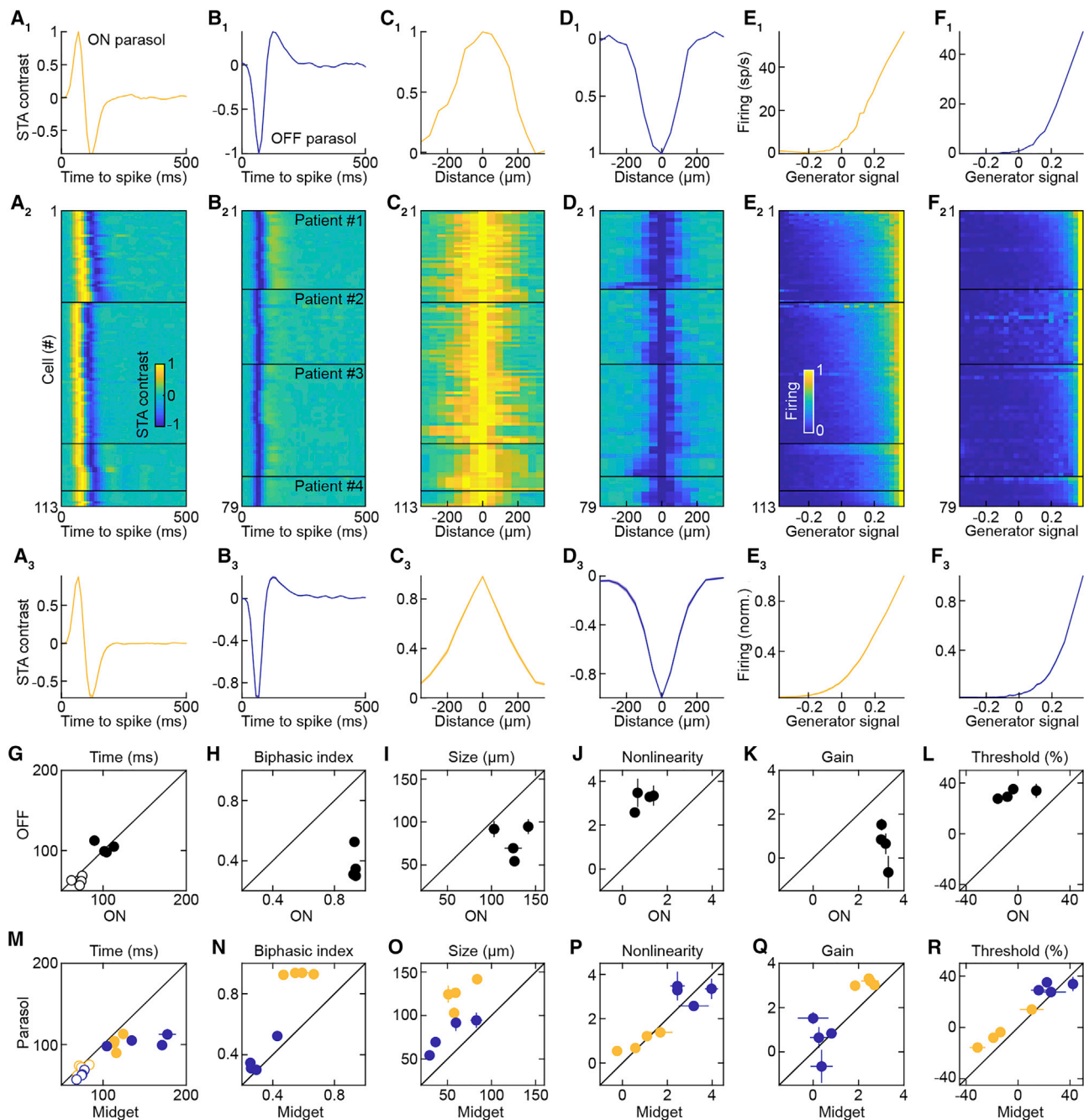


Figure 3. Functional Characterization of ON and OFF Parasol Ganglion Cells

(A₃–B₃) Temporal receptive fields of individual ON (A₁) and OFF (B₁) parasol ganglion cells, all ON (A₂) and OFF (B₂) parasol ganglion cells grouped by patients and sorted by their time to peak, and the average (±SEM) of all ON (A₃) and OFF (B₃) parasol ganglion cells.
(C₃–D₃) Spatial receptive fields of individual ON (C₁) and OFF (D₁) parasol ganglion cells, all ON (C₂) and OFF (D₂) parasol ganglion cells grouped by patients and sorted by their size, and the average (±SEM) of all ON (C₃) and OFF (D₃) parasol ganglion cells.
(E₃–F₃) Static nonlinearities (or effective-contrast-response functions) of individual ON (E₁) and OFF (F₁) parasol ganglion cells, all ON (E₂) and OFF (F₂) parasol ganglion cells grouped by patients and sorted by their threshold, and the average (±SEM) of all ON (E₃) and OFF (F₃) parasol ganglion cells.
(G–L) Summary data (mean ± SEM) comparing time to peak (G, TTP $p < 0.01$ except for patient 2, $\eta^2 = 0.22 \pm 0.14$, empty circles), time to zero crossing (G, TTZ $p \geq 0.05$ except for patient 2, $\eta^2 = 0.17 \pm 0.13$, filled circles), biphasic index (H, all $p < 0.001$, $\eta^2 = 0.66 \pm 0.04$), receptive field size (I, $p < 10^{-5}$ except for patient 4, $\eta^2 = 0.54 \pm 0.02$), nonlinearity (J, all $p < 0.01$, $\eta^2 = 0.64 \pm 0.02$), gain (K, all $p < 0.001$, $\eta^2 = 0.48 \pm 0.05$), and threshold (L, all $p < 0.05$, $\eta^2 = 0.63 \pm 0.02$) of ON versus OFF parasol ganglion cells.

(legend continued on next page)

transient responses (Suh and Baccus, 2014). In the mouse retina, bipolar cell axons with transient responses stratify in the center of the inner plexiform layer (IPL), whereas those with sustained responses stratify in the IPL periphery (Baden et al., 2013; Borghuis et al., 2013; Franke et al., 2017). Our observation that parasol ganglion cells, whose dendrites stratify in the middle of the IPL, have more biphasic receptive fields (Figure 2 and 3) and more transient responses than midget ganglion cells, whose dendrites stratify toward its edges (Figure S5), suggests that the centropolar map of temporal tuning in the IPL is conserved from rodents to humans (Euler et al., 2014).

Many spatiotemporal receptive field characteristics appear to be conserved between humans (Figures 2 and 3) and non-human primates (Chichilnisky, 2001; Chichilnisky and Kalmar, 2002; Crook et al., 2014). However, comparisons of our results to previous studies of macaques also reveal functional divergence. Notably, the temporal receptive fields of ON parasol ganglion cells in our study (Figure 3) are emphatically more biphasic than those reported for macaques (Chichilnisky and Kalmar, 2002). There is some uncertainty in comparing results across studies with similar but not identical stimulus and recording conditions. Nonetheless, we think the difference in the temporal receptive fields of ON parasol ganglion cells is significant for the following reasons. First, the difference is vast; Chichilnisky and Kalmar (2002) calculate the biphasic index of temporal receptive fields as $|trough/peak|$. This index is ~ 0.35 for ON parasol cells in macaques (Chichilnisky and Kalmar, 2002) compared to 0.91 ± 0.01 in humans (this study). Second, the difference is selective; the temporal receptive fields (including biphasic indices) of OFF parasol and ON and OFF midget ganglion cells from (Chichilnisky and Kalmar, 2002) closely align with those reported here. Third, the difference is consistent; results from all four patients in our study match and the temporal receptive fields of ON parasol ganglion cells in macaques are similar across studies conducted in different laboratories under different conditions (Ala-Laurila et al., 2011; Cafaro and Rieke, 2013; Chichilnisky and Kalmar, 2002; Field et al., 2007; Puller et al., 2015; Rhoades et al., 2019). Direct comparisons of visual psychophysics in humans and non-human primates are scarce and have not probed temporal tuning with stimuli isolating contributions of ON parasol ganglion cells (De Valois et al., 1974; Matsuno and Fujita, 2009). Therefore, it remains to be seen whether the differences in temporal receptive fields of ON parasol ganglion cells lead to differences in visual perception of humans and non-human primates.

Our results reveal a consistent relationship between the spatial and the temporal receptive fields of ON and OFF midget and ON and OFF parasol ganglion cells (Figures 2, 3, and 4). Across the four cell types, larger spatial receptive fields are associated with more biphasic temporal receptive fields and smaller spatial

receptive fields with more monophasic temporal receptive fields. Large spatial and monophasic temporal receptive fields allow low spatial and temporal stimulus frequencies, respectively, to drive neuronal activity. Because low frequencies abound in our visual environment (Dong and Atick, 1995; Pitkow and Meister, 2012; Simoncelli and Olshausen, 2001), we reasoned that the inverse correlation between spatial and temporal filters may reflect a fundamental tradeoff. Consistent with this idea, we found that spatiotemporal filters of ON and OFF midget and ON and OFF parasol ganglion cells occupy adjacent sections of an isopower line in the frequency landscape of naturalistic movies (Figure 4). We interpret these findings as follows: (1) differences in spatio-temporal filtering allow ON and OFF midget and ON and OFF parasol ganglion cells to encode distinct aspects of the visual environment and reduce redundancy between them (Barlow, 1961, 2001); (2) their adjacent positions enable them to cover a behaviorally relevant area of frequency space jointly; and (3) tradeoffs between spatial and temporal filters of individual cell types distribute stimulus power equally between them. Intriguingly, convolutional neural networks optimized to encode naturalistic movies in ganglion cell spike trains with a limited firing rate budget (Ocko et al., 2018) give rise to four cell types with spatiotemporal receptive fields closely resembling ON and OFF midget and ON and OFF parasol ganglion cells (Figures 2 and 3). This convergence suggests that evolution found a near-optimal solution for filtering visual inputs.

Shortly after its identification, the split into paired ON and OFF channels was suggested to reduce the number of spikes needed to encode stimulus distributions (Schiller et al., 1986), a notion supported and elaborated by subsequent computational modeling (Gjorgjieva et al., 2014, 2019). Here, we identify consistent asymmetries in the contrast-response functions of paramorphic ON and OFF cells. Specifically, the contrast-response functions of ON midget and ON parasol ganglion cells in the human retina have lower thresholds, higher gain, and are more linear than those of their OFF counterparts (Figures 2, 3, and S5). Indeed, in our recordings, differences in contrast sensitivity were more pronounced between paramorphic ON and OFF types than between midget and parasol ganglion cells (Figure S5). Li et al. (2014) found that midget and parasol ganglion cells respond similarly to stimulation of individual cones and that differences in their sensitivity to larger stimuli can be accounted for by differences in cone-convergence (i.e., receptive field size). In our recordings (eccentricities: 18° – 38° or 5–10 mm), differences in receptive field size of parasol and midget ganglion cells were small (parasol:midget $\sim 2:1$). Differences in dendritic field sizes of midget and parasol ganglion cells increase steeply from the periphery (parasol:midget $\sim 3:1$) to the fovea (parasol:midget $\sim 30:1$) (Dacey and Petersen, 1992). We, therefore, expect differences in contrast sensitivity between human

(M–R) Summary data (mean \pm SEM) comparing time to peak (M, TTP, ON $p < 0.01$ except for patients 3 and 4, $\eta^2 = 0.14 \pm 0.05$, OFF all $p < 0.01$, $\eta^2 = 0.40 \pm 0.04$, empty circles), time to zero crossing (M, TTZ, ON all $p < 0.01$ except for patient 4, $\eta^2 = 0.35 \pm 0.16$, OFF all $p < 10^{-4}$, $\eta^2 = 0.65 \pm 0.06$, filled circles), biphasic index (N, ON all $p < 0.01$, $\eta^2 = 0.65 \pm 0.03$, OFF $p < 0.01$ except for patients 2 and 4, $\eta^2 = 0.20 \pm 0.08$), receptive field size (O, ON all $p < 0.001$, $\eta^2 = 0.61 \pm 0.02$, OFF all $p < 0.05$ except for patients 1 and 4, $\eta^2 = 0.34 \pm 0.18$), nonlinearity (P, ON $p > 0.4$ except for patient 1 $p < 0.001$, $\eta^2 = 0.12 \pm 0.11$, OFF $p < 0.05$ except for patient 1, $\eta^2 = 0.14 \pm 0.06$), gain (Q, ON all $p < 10^{-5}$ except for patients 1 and 4, $\eta^2 = 0.22 \pm 0.09$, OFF $p > 0.2$ except for patient 1 $p < 0.05$, $\eta^2 = 0.09 \pm 0.06$), and threshold (R, ON all $p < 0.05$ except for patient 4, $\eta^2 = 0.10 \pm 0.02$, OFF $p < 0.05$ except for patients 1 and 4, $\eta^2 = 0.16 \pm 0.08$) of midget versus parasol ganglion cells. See also Figures S3 and S4.

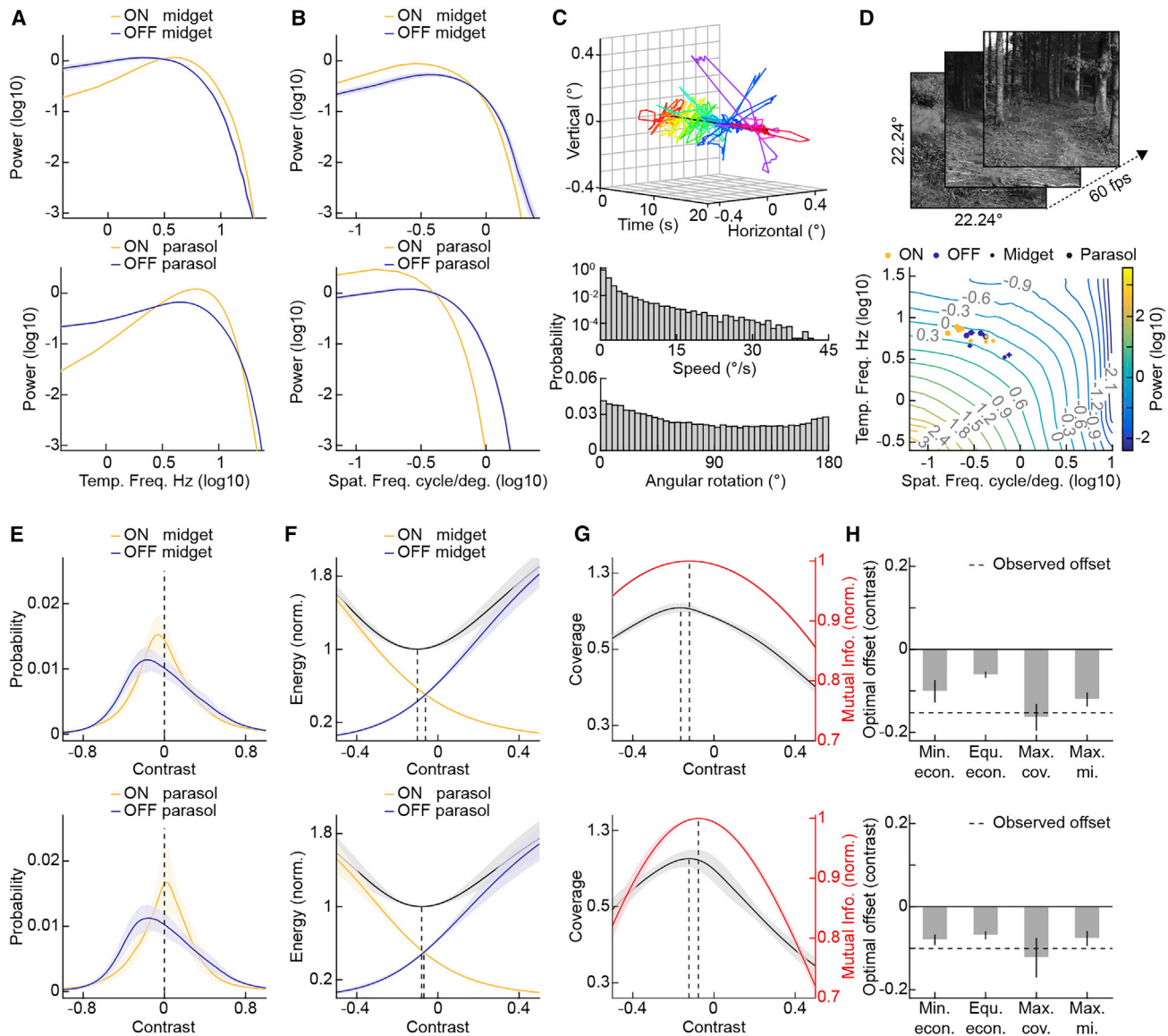


Figure 4. Midget and Parasol Ganglion Cells Efficiently Encode Luminance Contrast in Naturalistic Movies

(A and B) Temporal (A) and spatial (B) frequency-domain filters of ON and OFF midget (top row) and ON and OFF parasol ganglion cells (bottom row). Solid lines (shaded areas) represent the mean (\pm SEM) of all cells of a given type.

(C) Top panel: representative fixational eye movement trajectory applied to a movie clip. The trajectory is composed of 63 randomly chosen and concatenated episodes (total duration: 20 s) and is color-coded to indicate the passage of time (shown along the x axis). Each episode contains eye movements (shown along the y- and z-axes) during a period of fixation from the DOVES eye movement dataset (Van Der Linde et al., 2009). The center of the fixation is indicated by a black line through the trajectory. Bottom panel: probability distributions of the speed ($^{\circ}$ of visual angle/s) and angular rotation ($^{\circ}$ of change in gaze movement direction) for all fixational eye movements applied to our naturalistic movies.

(D) Representative frames (top panel) and spatiotemporal frequency decomposition (bottom panel) of naturalistic movies. In the bottom panel, isopower lines are color-coded, and the positions of the centers of mass of the filters (mean \pm SEM) for ON and OFF midget (small circles) and ON and OFF parasol ganglion cells (large circles) from each patient are indicated.

(E) Contrast distributions of naturalistic movies (mean \pm SD, $n = 33$ movies) convolved with spatiotemporal receptive fields of ON and OFF midget (top) and ON and OFF parasol ganglion cells (bottom). Dashed lines indicate contrast = 0.

(F) Energy cost (i.e., proportional to firing rates) of encoding stimulus distributions as a function of varying contrast offsets in the intersections of ON and OFF response functions for midget (top) and parasol ganglion cells (bottom). The combined energy costs of ON and OFF cells are shown by solid black lines (mean) and gray shaded areas (\pm SD). Dashed lines indicate contrast offsets for equal energy cost of ON and OFF cells and the combined minimum.

(G) Stimulus coverage (black) and mutual information (red) as a function of varying contrast offsets in the intersection of ON and OFF response functions for midget (top) and parasol ganglion cells (bottom). Solid lines (shaded areas) indicate the mean (\pm SD) for the encoding of 10 naturalistic movies. Dashed lines indicate contrast offsets for maximal coverage and maximal mutual information.

(legend continued on next page)

midget and parasol ganglion cells, similar to those observed in macaques (Kaplan and Shapley, 1986), to emerge toward the fovea. Future studies of humans and non-human primates should map contrast sensitivities across the retina to test whether differences between ON versus OFF types and midget versus parasol ganglion cells dominate in different retinal domains.

In macaques, ON-OFF asymmetries have been reported for parasol ganglion cells (Chichilnisky and Kalmar, 2002; Turner and Rieke, 2016) but remain unexplored for midget ganglion cells. As part of the ON-OFF asymmetries in humans, we observe high contrast sensitivity for ON midget cells in the peripheral retina. If this is not recapitulated in the macaques, it may contribute to the greater perceptual contrast sensitivity of humans and its shallower decline in the peripheral visual field compared to macaques (Sasaoka et al., 2005). We speculate that ON-OFF asymmetries in the contrast-response functions arise in part from differences in the rectification of ON and OFF bipolar cells (Borghuis et al., 2013; Turner and Rieke, 2016) caused by prominent ON-to-OFF crossover inhibition between them (Akrouh and Kerschensteiner, 2013; Liang and Freed, 2010; Manookin et al., 2008).

Efficient coding theory predicts that, in addition to reducing redundancy between neurons, sensory systems should transmit maximal information about our environment with the fewest spikes possible (i.e., minimal metabolic cost) (Attneave, 1954; Barlow, 1961; Lindsey et al., 2019; Pitkow and Meister, 2012; Turner et al., 2019). We find that in conjunction with their spatio-temporal receptive fields, asymmetric contrast-response functions of ON and OFF midget and ON and OFF parasol ganglion cells maximize stimulus coverage and information transmission while minimizing the required energy (Figure 4). One caveat to our findings is that the retinal processing of naturalistic stimuli may deviate from that of white noise stimuli. This should be explored in future studies, when compact models that can predict neural responses to naturalistic stimuli have been developed (Heitman et al., 2016). The current efficient coding framework assumes that a veridical representation of the environment is a goal of retinal processing. This assumption is justified for midget and parasol ganglion cells by (1) their light responses (Figures 2, 3, 4, and S4), (2) their projection patterns and downstream pathways (Nassi and Callaway, 2009; Van Essen et al., 1992), and (3) the deficits incurred from lesions to midget and parasol ganglion cells or their downstream pathways (Merigan and Eskin, 1986; Merigan et al., 1991b, 1991a). However, the same assumption is likely incorrect for ganglion cell types that act as feature detectors (Gollisch and Meister, 2010). Efforts are underway to extend the efficient coding framework to all ganglion cell types by implementing goal-oriented optimizations inspired by behavioral demands (Turner et al., 2019). The success of efficient coding in explaining the full complement of output signals from the retina remains to be determined as does its generalization to other senses (Smith and Lewicki, 2006; Teşileanu et al., 2019; Uchida

et al., 2014). For now, we provide insights into the sensory transformations in the primary parallel pathways from our eyes to our brain with important implications for downstream visual processing, psychophysics, and the design of machine vision systems.

STAR★METHODS

Detailed methods are provided in the online version of this paper and include the following:

- KEY RESOURCES TABLE
- RESOURCE AVAILABILITY
 - Lead Contact
 - Materials Availability
 - Data and Code Availability
- EXPERIMENTAL MODEL AND SUBJECT DETAILS
 - Patients
- METHOD DETAILS
 - Retina Preparation
 - Multielectrode Array Recordings
 - Light Stimulation
 - Functional Classification of Ganglion Cells
 - Power Spectrum Analysis of Naturalistic Movies
 - Analysis of Fixational Eye Movements
 - Power Spectrum Analysis of Receptive Fields
 - Effective Contrast Distributions of Naturalistic Movies
 - Energy Consumption Analysis
 - Stimulus Coverage Analysis
 - Mutual Information Analysis
- QUANTIFICATION AND STATISTICAL ANALYSIS

SUPPLEMENTAL INFORMATION

Supplemental Information can be found online at <https://doi.org/10.1016/j.neuron.2020.05.030>.

ACKNOWLEDGMENTS

We are grateful to the patients who participated in this study. We thank Drs. F. Rieke and A.V. Kolesnikov for advice on tissue preparation. We thank members of the Kerschensteiner lab for helpful discussions throughout this study. This work was supported by the NIH (EY027411 to F.S. and D.K., EY030623 to J.L.M. and D.K., EY023441 and EY026978 to D.K., and EY002687 to the Department of Ophthalmology and Visual Sciences), the Grace Nelson Lacy Research Fund (director: D.K.), and an unrestricted grant to the Department of Ophthalmology and Visual Sciences from Research to Prevent Blindness.

AUTHOR CONTRIBUTIONS

F.S., J.-C.H., and D.K. conceived of this study. F.S., R.R., K.P., G.J.H., S.M.C., P.C., J.L.M., and D.K. procured and prepared the tissue. F.S. performed multi-electrode array recordings. F.S., J.-C.H., and D.K. analyzed data and wrote the manuscript with input from all authors.

(H) Contrast offsets in the intersections of ON and OFF response functions that minimize (Min. econ.) and equalize (Equ. econ.) energy consumption and maximize stimulus coverage (Max. cov.) and mutual information (Max. MI.) between naturalistic movies stimuli and a system of ON and OFF midget (top) and ON and OFF parasol ganglion cells (bottom). The experimentally observed contrast offsets are indicated by dashed lines. See also Figure S5.

DECLARATION OF INTERESTS

The authors declare no competing interests.

Received: January 16, 2020

Revised: April 24, 2020

Accepted: May 20, 2020

Published: June 12, 2020

REFERENCES

- Agaoğlu, M.N., and Chung, S.T.L. (2020). Exploration of the functional consequences of fixational eye movements in the absence of a fovea. *J. Vis.* **20**, 12.
- Akrouh, A., and Kerschensteiner, D. (2013). Intersecting circuits generate precisely patterned retinal waves. *Neuron* **79**, 322–334.
- Ala-Laurila, P., Greschner, M., Chichilnisky, E.J., and Rieke, F. (2011). Cone photoreceptor contributions to noise and correlations in the retinal output. *Nat. Neurosci.* **14**, 1309–1316.
- Attneave, F. (1954). Some informational aspects of visual perception. *Psychol. Rev.* **61**, 183–193.
- Awatramani, G.B., and Slaughter, M.M. (2000). Origin of transient and sustained responses in ganglion cells of the retina. *J. Neurosci.* **20**, 7087–7095.
- Baden, T., Berens, P., Bethge, M., and Euler, T. (2013). Spikes in mammalian bipolar cells support temporal layering of the inner retina. *Curr. Biol.* **23**, 48–52.
- Baden, T., Euler, T., and Berens, P. (2020). Understanding the retinal basis of vision across species. *Nat. Rev. Neurosci.* **21**, 5–20.
- Barlow, H. (1961). Possible Principles Underlying the Transformations of Sensory Messages. *Sensory Communication 1*, <https://doi.org/10.7551/mitpress/9780262518420.003.0013>.
- Barlow, H. (2001). Redundancy reduction revisited. *Network* **12**, 241–253.
- Binda, P., and Morrone, M.C. (2018). Vision During Saccadic Eye Movements. *Annu. Rev. Vis. Sci.* **4**, 193–213.
- Borghuis, B.G., Marvin, J.S., Looger, L.L., and Demb, J.B. (2013). Two-photon imaging of nonlinear glutamate release dynamics at bipolar cell synapses in the mouse retina. *J. Neurosci.* **33**, 10972–10985.
- Brown, S.P., He, S., and Masland, R.H. (2000). Receptive field microstructure and dendritic geometry of retinal ganglion cells. *Neuron* **27**, 371–383.
- Cafaro, J., and Rieke, F. (2013). Regulation of spatial selectivity by crossover inhibition. *J. Neurosci.* **33**, 6310–6320.
- Chalasan, S.H., Chronis, N., Tsubozaki, M., Gray, J.M., Ramot, D., Goodman, M.B., and Bargmann, C.I. (2007). Dissecting a circuit for olfactory behaviour in *Caenorhabditis elegans*. *Nature* **450**, 63–70.
- Chichilnisky, E.J. (2001). A simple white noise analysis of neuronal light responses. *Network* **12**, 199–213.
- Chichilnisky, E.J., and Baylor, D.A. (1999). Receptive-field microstructure of blue-yellow ganglion cells in primate retina. *Nat. Neurosci.* **2**, 889–893.
- Chichilnisky, E.J., and Kalmar, R.S. (2002). Functional asymmetries in ON and OFF ganglion cells of primate retina. *J. Neurosci.* **22**, 2737–2747.
- Cover, T.M., and Thomas, J.A. (2012). *Elements of Information Theory* (John Wiley & Sons).
- Croner, L.J., and Kaplan, E. (1995). Receptive fields of P and M ganglion cells across the primate retina. *Vision Res.* **35**, 7–24.
- Cronin, T.W., Johnsen, S., Justin Marshall, N., and Warrant, E.J. (2014). *Visual Ecology* (Princeton University Press).
- Crook, J.D., Packer, O.S., and Dacey, D.M. (2014). A synaptic signature for ON- and OFF-center parasol ganglion cells of the primate retina. *Vis. Neurosci.* **31**, 57–84.
- Dacey, D.M. (1993). The mosaic of midget ganglion cells in the human retina. *J. Neurosci.* **13**, 5334–5355.
- Dacey, D.M. (2004). Origins of perception: retinal ganglion cell diversity and the creation of parallel visual pathways. *Cogn. Neurosci.* **3**, 281–301.
- Dacey, D.M., and Lee, B.B. (1994). The ‘blue-on’ opponent pathway in primate retina originates from a distinct bistratified ganglion cell type. *Nature* **367**, 731–735.
- Dacey, D.M., and Petersen, M.R. (1992). Dendritic field size and morphology of midget and parasol ganglion cells of the human retina. *Proc. Natl. Acad. Sci. USA* **89**, 9666–9670.
- Dacey, D., Packer, O.S., Diller, L., Brainard, D., Peterson, B., and Lee, B. (2000). Center surround receptive field structure of cone bipolar cells in primate retina. *Vision Res.* **40**, 1801–1811.
- de Monasterio, F.M. (1978). Properties of ganglion cells with atypical receptive-field organization in retina of macaques. *J. Neurophysiol.* **41**, 1435–1449.
- De Valois, R.L., Morgan, H., and Snodderly, D.M. (1974). Psychophysical studies of monkey vision. 3. Spatial luminance contrast sensitivity tests of macaque and human observers. *Vision Res.* **14**, 75–81.
- Delorme, A., Richard, G., and Fabre-Thorpe, M. (2000). Ultra-rapid categorisation of natural scenes does not rely on colour cues: a study in monkeys and humans. *Vision Res.* **40**, 2187–2200.
- Diamond, J.S., and Copenhagen, D.R. (1995). The relationship between light-evoked synaptic excitation and spiking behaviour of salamander retinal ganglion cells. *J. Physiol.* **487**, 711–725.
- Disotell, T.R., and Tosi, A.J. (2007). The monkey’s perspective. *Genome Biol.* **8**, 226.
- Dong, D.W., and Atick, J.J. (1995). Statistics of natural time-varying images. *Network* **6**, 345–358.
- Drasdo, N., and Fowler, C.W. (1974). Non-linear projection of the retinal image in a wide-angle schematic eye. *Br. J. Ophthalmol.* **58**, 709–714.
- Euler, T., Haverkamp, S., Schubert, T., and Baden, T. (2014). Retinal bipolar cells: elementary building blocks of vision. *Nat. Rev. Neurosci.* **15**, 507–519.
- Famiglietti, E.V. (2004). Class I and class II ganglion cells of rabbit retina: a structural basis for X and Y (brisk) cells. *J. Comp. Neurol.* **478**, 323–346.
- Field, G.D., and Chichilnisky, E.J. (2007). Information processing in the primate retina: circuitry and coding. *Annu. Rev. Neurosci.* **30**, 1–30.
- Field, G.D., Sher, A., Gauthier, J.L., Greschner, M., Shlens, J., Litke, A.M., and Chichilnisky, E.J. (2007). Spatial properties and functional organization of small bistratified ganglion cells in primate retina. *J. Neurosci.* **27**, 13261–13272.
- Field, G.D., Gauthier, J.L., Sher, A., Greschner, M., Machado, T.A., Jepson, L.H., Shlens, J., Gunning, D.E., Mathieson, K., Dabrowski, W., et al. (2010). Functional connectivity in the retina at the resolution of photoreceptors. *Nature* **467**, 673–677.
- Franke, K., Berens, P., Schubert, T., Bethge, M., Euler, T., and Baden, T. (2017). Inhibition decorrelates visual feature representations in the inner retina. *Nature* **542**, 439–444.
- Gallio, M., Ofstad, T.A., Macpherson, L.J., Wang, J.W., and Zuker, C.S. (2011). The coding of temperature in the *Drosophila* brain. *Cell* **144**, 614–624.
- Gjorgjieva, J., Sompolinsky, H., and Meister, M. (2014). Benefits of pathway splitting in sensory coding. *J. Neurosci.* **34**, 12127–12144.
- Gjorgjieva, J., Meister, M., and Sompolinsky, H. (2019). Functional diversity among sensory neurons from efficient coding principles. *PLoS Comput. Biol.* **15**, e1007476.
- Gollisch, T., and Meister, M. (2010). Eye smarter than scientists believed: neural computations in circuits of the retina. *Neuron* **65**, 150–164.
- Grimes, W.N., Songco-Aguas, A., and Rieke, F. (2018). Parallel Processing of Rod and Cone Signals: Retinal Function and Human Perception. *Annu. Rev. Vis. Sci.* **4**, 123–141.
- Heitman, A., Brackbill, N., Greschner, M., Sher, A., and Litke, A.M. (2016). Testing pseudo-linear models of responses to natural scenes in primate retina. *bioRxiv*. <https://doi.org/10.1101/045336>.
- Holmes, C.M., and Nemenman, I. (2019). Estimation of mutual information for real-valued data with error bars and controlled bias. *Phys. Rev. E* **100**, 022404.

- Hurley, J.B., Ebrey, T.G., Honig, B., and Ottolenghi, M. (1977). Temperature and wavelength effects on the photochemistry of rhodopsin, isorhodopsin, bacteriorhodopsin and their photoproducts. *Nature* 270, 540–542.
- Joesch, M., Schnell, B., Raghu, S.V., Reiff, D.F., and Borst, A. (2010). ON and OFF pathways in *Drosophila* motion vision. *Nature* 468, 300–304.
- Ju, H., Hines, M.L., and Yu, Y. (2016). Cable energy function of cortical axons. *Sci. Rep.* 6, 29686.
- Kaplan, E. (2008). Luminance sensitivity and contrast detection. In *The Senses: A Comprehensive Reference*, Masland, R.H., Albright, T.D., Dallos, P., Oertel, D., Firestein, S., G.K. Beauchamp, M.C. Bushnell, A.I. Basbaum, J.H. Kaas, and E.P. Gardner, eds. (Elsevier), pp. 29–43.
- Kaplan, E., and Shapley, R.M. (1986). The primate retina contains two types of ganglion cells, with high and low contrast sensitivity. *Proc. Natl. Acad. Sci. USA* 83, 2755–2757.
- Kingdom, F.A.A., and Prins, N. (2016). *Psychophysics: A Practical Introduction* (Academic Press).
- Kolb, H., and Marshak, D. (2003). The midget pathways of the primate retina. *Doc. Ophthalmol.* 106, 67–81.
- Kolesnikov, A.V., Tang, P.H., and Kefalov, V.J. (2018). Examining the Role of Cone-expressed RPE65 in Mouse Cone Function. *Sci. Rep.* 8, 14201.
- Kraskov, A., Stögbauer, H., and Grassberger, P. (2004). Estimating mutual information. *Phys. Rev. E Stat. Nonlin. Soft Matter Phys.* 69, 066138.
- Li, P.H., Field, G.D., Greschner, M., Ahn, D., Gunning, D.E., Mathieson, K., Sher, A., Litke, A.M., and Chichilnisky, E.J. (2014). Retinal representation of the elementary visual signal. *Neuron* 81, 130–139.
- Liang, Z., and Freed, M.A. (2010). The ON pathway rectifies the OFF pathway of the mammalian retina. *J. Neurosci.* 30, 5533–5543.
- Lindsey, J., Ocko, S.A., Ganguli, S., and Deny, S. (2019). A Unified Theory of Early Visual Representations from Retina to Cortex through Anatomically Constrained Deep CNNs. *bioRxiv*. <https://doi.org/10.1101/511535>.
- Manookin, M.B., Beaudoin, D.L., Ernst, Z.R., Flagel, L.J., and Domb, J.B. (2008). Disinhibition combines with excitation to extend the operating range of the OFF visual pathway in daylight. *J. Neurosci.* 28, 4136–4150.
- Manookin, M.B., Patterson, S.S., and Linehan, C.M. (2018). Neural Mechanisms Mediating Motion Sensitivity in Parasol Ganglion Cells of the Primate Retina. *Neuron* 97, 1327–1340.
- Martin, P.R., Lee, B.B., White, A.J., Solomon, S.G., and Rüttiger, L. (2001). Chromatic sensitivity of ganglion cells in the peripheral primate retina. *Nature* 410, 933–936.
- Masri, R.A., Lee, S.C.S., Madigan, M.C., and Grünert, U. (2019a). Particle-Mediated Gene Transfection and Organotypic Culture of Postmortem Human Retina. *Transl. Vis. Sci. Technol.* 8, 7.
- Masri, R.A., Percival, K.A., Koizumi, A., Martin, P.R., and Grünert, U. (2019b). Survey of retinal ganglion cell morphology in marmoset. *J. Comp. Neurol.* 527, 236–258.
- Matsuno, T., and Fujita, K. (2009). A comparative psychophysical approach to visual perception in primates. *Primates* 50, 121–130.
- Meister, M. (2003). Adaptation of the retinal code: what the eye does not tell the brain. In *The Neural Basis of Early Vision*, A. Kaneko, ed. (Springer), p. 61.
- Merigan, W.H., and Eskin, T.A. (1986). Spatio-temporal vision of macaques with severe loss of P beta retinal ganglion cells. *Vision Res.* 26, 1751–1761.
- Merigan, W.H., Katz, L.M., and Maunsell, J.H. (1991a). The effects of parvocellular lateral geniculate lesions on the acuity and contrast sensitivity of macaque monkeys. *J. Neurosci.* 11, 994–1001.
- Merigan, W.H., Byrne, C.E., and Maunsell, J.H. (1991b). Does primate motion perception depend on the magnocellular pathway? *J. Neurosci.* 11, 3422–3429.
- Murphy, G.J., and Rieke, F. (2011). Electrical synaptic input to ganglion cells underlies differences in the output and absolute sensitivity of parallel retinal circuits. *J. Neurosci.* 31, 12218–12228.
- Nassi, J.J., and Callaway, E.M. (2009). Parallel processing strategies of the primate visual system. *Nat. Rev. Neurosci.* 10, 360–372.
- Ocko, S., Lindsey, J., Ganguli, S., and Deny, S. (2018). The emergence of multiple retinal cell types through efficient coding of natural movies. In *Advances in Neural Information Processing Systems 31*, S. Bengio, H. Wallach, H. Larochelle, K. Grauman, N. Cesa-Bianchi, and R. Garnett, eds. (Curran Associates, Inc.), pp. 9389–9400.
- Pearson, J.T., and Kerschensteiner, D. (2015). Ambient illumination switches contrast preference of specific retinal processing streams. *J. Neurophysiol.* 114, 540–550.
- Peichl, L., and Wässle, H. (1983). The structural correlate of the receptive field centre of alpha ganglion cells in the cat retina. *J. Physiol.* 341, 309–324.
- Pitkow, X., and Meister, M. (2012). Decorrelation and efficient coding by retinal ganglion cells. *Nat. Neurosci.* 15, 628–635.
- Puller, C., Manookin, M.B., Neitz, J., Rieke, F., and Neitz, M. (2015). Broad thorny ganglion cells: a candidate for visual pursuit error signaling in the primate retina. *J. Neurosci.* 35, 5397–5408.
- Puthussery, T., Percival, K.A., Venkataramani, S., Gayet-Primo, J., Grünert, U., and Taylor, W.R. (2014). Kainate receptors mediate synaptic input to transient and sustained OFF visual pathways in primate retina. *J. Neurosci.* 34, 7611–7621.
- Ravi, S., Ahn, D., Greschner, M., Chichilnisky, E.J., and Field, G.D. (2018). Pathway-Specific Asymmetries between ON and OFF Visual Signals. *J. Neurosci.* 38, 9728–9740.
- Rhoades, C.E., Shah, N.P., Manookin, M.B., Brackbill, N., Kling, A., Goetz, G., Sher, A., Litke, A.M., and Chichilnisky, E.J. (2019). Unusual Physiological Properties of Smooth Monostriated Ganglion Cell Types in Primate Retina. *Neuron* 103, 658–672.
- Sabesan, R., Schmidt, B.P., Tuten, W.S., and Roorda, A. (2016). The elementary representation of spatial and color vision in the human retina. *Sci. Adv.* 2, e1600797.
- Saha, D., Leong, K., Li, C., Peterson, S., Siegel, G., and Raman, B. (2013). A spatiotemporal coding mechanism for background-invariant odor recognition. *Nat. Neurosci.* 16, 1830–1839.
- Sasaoka, M., Hara, H., and Nakamura, K. (2005). Comparison between monkey and human visual fields using a personal computer system. *Behav. Brain Res.* 161, 18–30.
- Saunders, J., and Bastian, J. (1984). The physiology and morphology of two types of electrosensory neurons in the weakly electric fish *Apteronotus leptorhynchus*. *J. Comp. Physiol. A Neuroethol. Sens. Neural Behav. Physiol.* 154, 199–209.
- Schiller, P.H., Sandell, J.H., and Maunsell, J.H.R. (1986). Functions of the ON and OFF channels of the visual system. *Nature* 322, 824–825.
- Scholl, B., Gao, X., and Wehr, M. (2010). Nonoverlapping sets of synapses drive on responses and off responses in auditory cortex. *Neuron* 65, 412–421.
- Schwartz, G.W., Okawa, H., Dunn, F.A., Morgan, J.L., Kerschensteiner, D., Wong, R.O., and Rieke, F. (2012). The spatial structure of a nonlinear receptive field. *Nat. Neurosci.* 15, 1572–1580.
- Sekharan, S., and Morokuma, K. (2011). Why 11-cis-retinal? Why not 7-cis-, 9-cis-, or 13-cis-retinal in the eye? *J. Am. Chem. Soc.* 133, 19052–19055.
- Simoncelli, E.P. (2003). Vision and the statistics of the visual environment. *Curr. Opin. Neurobiol.* 13, 144–149.
- Simoncelli, E.P., and Olshausen, B.A. (2001). Natural image statistics and neural representation. *Annu. Rev. Neurosci.* 24, 1193–1216.
- Sinha, R., Hoon, M., Baudin, J., Okawa, H., Wong, R.O.L., and Rieke, F. (2017). Cellular and Circuit Mechanisms Shaping the Perceptual Properties of the Primate Fovea. *Cell* 168, 413–426.
- Smith, E.C., and Lewicki, M.S. (2006). Efficient auditory coding. *Nature* 439, 978–982.
- Springer, M.S., Murphy, W.J., Eizirik, E., and O'Brien, S.J. (2003). Placental mammal diversification and the Cretaceous-Tertiary boundary. *Proc. Natl. Acad. Sci. USA* 100, 1056–1061.
- Stone, L.S., Watson, A.B., and Mulligan, J.B. (1990). Effect of contrast on the perceived direction of a moving plaid. *Vision Res.* 30, 1049–1067.

- Suh, B., and Baccus, S.A. (2014). Building blocks of temporal filters in retinal synapses. *PLoS Biol.* *12*, e1001973.
- Teşileanu, T., Cocco, S., Monasson, R., and Balasubramanian, V. (2019). Adaptation of olfactory receptor abundances for efficient coding. *eLife* *8*, e39279.
- Tien, N.-W., Pearson, J.T., Heller, C.R., Demas, J., and Kerschensteiner, D. (2015). Genetically Identified Suppressed-by-Contrast Retinal Ganglion Cells Reliably Signal Self-Generated Visual Stimuli. *J. Neurosci.* *35*, 10815–10820.
- Turner, M.H., and Rieke, F. (2016). Synaptic Rectification Controls Nonlinear Spatial Integration of Natural Visual Inputs. *Neuron* *90*, 1257–1271.
- Turner, M.H., Sanchez Giraldo, L.G., Schwartz, O., and Rieke, F. (2019). Stimulus- and goal-oriented frameworks for understanding natural vision. *Nat. Neurosci.* *22*, 15–24.
- Uchida, N., Poo, C., and Haddad, R. (2014). Coding and transformations in the olfactory system. *Annu. Rev. Neurosci.* *37*, 363–385.
- Van Der Linde, I., Rajashekar, U., Bovik, A.C., and Cormack, L.K. (2009). DOVES: a database of visual eye movements. *Spat. Vis.* *22*, 161–177.
- van der Maaten, L., and Hinton, G. (2008). Visualizing Data using t-SNE. *J. Mach. Learn. Res.* *9*, 2579–2605.
- Van Essen, D.C., Anderson, C.H., and Felleman, D.J. (1992). Information processing in the primate visual system: an integrated systems perspective. *Science* *255*, 419–423.
- Wässle, H., Grünert, U., Martin, P.R., and Boycott, B.B. (1994). Immunocytochemical characterization and spatial distribution of midget bipolar cells in the macaque monkey retina. *Vision Res.* *34*, 561–579.
- Weinstein, G.W., Hobson, R.R., and Baker, F.H. (1971). Extracellular recordings from human retinal ganglion cells. *Science* *171*, 1021–1022.
- Wool, L.E., Crook, J.D., Troy, J.B., Packer, O.S., Zaidi, Q., and Dacey, D.M. (2018). Nonselective Wiring Accounts for Red-Green Opponency in Midget Ganglion Cells of the Primate Retina. *J. Neurosci.* *38*, 1520–1540.
- Yang, G., and Masland, R.H. (1992). Direct visualization of the dendritic and receptive fields of directionally selective retinal ganglion cells. *Science* *258*, 1949–1952.

STAR★METHODS

KEY RESOURCES TABLE

REAGENT or RESOURCE	SOURCE	IDENTIFIER
Biological Samples		
Human retina, male, 78 years.	This paper	Patient ID # 70919
Human retina, female, 79 years.	This paper	Patient ID # 72319
Human retina, male, 68 years.	This paper	Patient ID # 73019
Human retina, male, 73 years.	This paper	Patient ID # 31720
Chemicals, Peptides, and Recombinant Proteins		
Ames' medium	Millipore Sigma	Cat # A1420
Hyaluronidase, type V	Millipore Sigma	Cat # H6254
9-cis retinal	Millipore Sigma	Cat # R5754
Bovine serum albumin	Millipore Sigma	Cat # A7030
Software and Algorithms		
MATLAB	Mathworks	RRID:SCR_001622
Cogent Graphics Toolbox	Laboratory of Neurobiology	http://www.vislab.ucl.ac.uk
MC_Rack	Smart Ephys	RRID:SCR_014955
Offline Sorter	Plexon Inc.	RRID:SCR_000012
Other		
Multielectrode array recording system	Smart Ephys	USB-MEA256-System
Multielectrode arrays	Smart Ephys	256MEA100/30iR-ITO

RESOURCE AVAILABILITY

Lead Contact

Information and requests for resources and reagents should be directed to and will be fulfilled by the Lead Contact, Daniel Kerschensteiner (kerschensteinerd@wustl.edu).

Materials Availability

This study did not generate new unique reagents.

Data and Code Availability

The datasets and code supporting the current study have not been deposited in a public repository because of their size and the extensive user experience required to navigate them. They are available from the Lead Contact on request.

EXPERIMENTAL MODEL AND SUBJECT DETAILS

Patients

Retinas were obtained from three treatment-naive patients enucleated for choroidal malignant melanomas (CMMs). Patient ID# 70919 (i.e., Patient #1): 78-year-old male, CMM right eye, intraocular pressure (IOP) 10 mmHg, medication of Tramadol 50 mg qd, Omeprazole 20 mg qd, Naproxen 220 qd, and Multivitamin. Patient ID# 72319 (i.e., Patient #2): 79-year-old female, CMM left eye, IOP 15 mmHg, medication of Anastrozole 1 tab qd; Ascorbic acid 500 mg qd; Biotin 5 mg qd; Cholecalciferol 5000 U qd; Carvedilol 6.25 mg qd; Furosemide 40 mg qd. Patient ID# 73019 (i.e., Patient #3): 68-year-old male, CMM right eye, IOP 12 mmHg, no medication. Patient ID# 31720 (i.e., Patient #4): 73-year-old male, CMM right eye, Atorvastatin 40 mg qd, Levothyroxine 75 mcg qd. The research protocol for this study was approved by the Washington University School of Medicine Human Research Protection Office and the Institutional Review Board (IRB, Protocol #201805087) in compliance with HIPAA guidelines and the tenets of the Declaration of Helsinki. Written informed consent was obtained from the patients prior to inclusion in the study.

METHOD DETAILS

Retina Preparation

Within 5 min of central artery occlusion, eyes were bisected under transillumination with a sterile razor blade (Figure 1A) on the non-tumor side of the optic nerve. The non-tumor-side eyecup was then transported from the operating room to the laboratory (~10 min) in a dark container filled with oxygenated HEPES-buffered Ames' medium (10 mM HEPES, equilibrated to pH 7.4 with NaOH, and containing 10 mg / mL hyaluronidase). Hyaluronidase was included to remove the vitreous. In control experiments in mice, we confirmed that exposure to hyaluronidase does not affect retinal health or light responses. All subsequent steps were performed under infrared illumination. The eyecup preparation was transferred into HEPES-buffered Ames' medium with 130 μ M 9-*cis* retinal and 1% BSA (pH adjusted to 7.4 with NaOH) and allowed to dark adapt and oxygenated for > 1hr at room temperature. Following dark adaptation, we isolated the retina from the pigment epithelium and any residual vitreous and mounted rectangular pieces on multi-electrode arrays. Based on our dissections, the branching patterns and diameters of retinal blood vessels, and the receptive field diameters across the four ganglion cell types we characterized, we estimate that the recording from Patient #1 was centered at 8-10 mm (30-38°) eccentricity, the recordings from Patients #2 and #3 were centered at 5-6 mm (18-22°) eccentricity, and the recording from Patient #4 was centered at 6-7 mm (22-26°) eccentricity.

Multielectrode Array Recordings

Rectangular pieces (~2 × 3 mm) of retina were mounted ganglion cell-side down on planar arrays of 252 electrodes (electrode diameter: 30 μ m, center-center spacing: 100 μ m) in a 16 × 16 grid with the four corner positions empty (Multichannel Systems). Retinas were secured on the arrays with a transparent membrane (3- μ m pore size, Corning) weighed down by a platinum ring. During recordings, retinas were superfused with warm (31°-34° C) bicarbonate-buffered Ames medium (equilibrated with 95% O₂ 5% CO₂) at a rate of 6-8 mL/min. The signal of each electrode was bandpass filtered between 300-3000 Hz and digitized at 10 kHz. Signal cut-outs from 1 ms before to 2 ms after crossings of negative thresholds (set manually for each channel) were recorded to hard disk together with the time of threshold crossing (i.e., spike time). Principal component analysis of these waveforms was used to sort spikes into trains representing the activity of individual neurons (Offline Sorter, Plexon Inc.). The quality of spike sorting was assessed by refractory periods and only spike trains with < 0.2% of interspike intervals < 2 ms retained. Cross-correlations of spike trains were computed to detect when activity from a single neuron had been recorded on more than one electrode. In these cases, only the trains with the most spikes were used for further analysis.

Light Stimulation

Light stimuli were presented on an organic light-emitting display (OLED-XL, eMagin) and focused onto the retina through a 20X 0.5 NA water immersion objective (Olympus). Stimuli were generated in MATLAB using the Cogent Graphics toolbox extensions developed by John Romaya at the Laboratory of Neurobiology at the Wellcome Department of Imaging Neuroscience and the display output linearized with custom-written scripts. All stimuli in this study modulated light as achromatic RGB triplets. The photopigments in our recordings were a mixture of 11-*cis* retinal (endogenous recovery) and 9-*cis* retinal (exogenous supplementation). The average intensity was constant across all stimuli. Photoisomerization rates at this intensity were between ~12,500 rhodopsin isomerization per rod per second (R*) for 11-*cis* retinal and ~3,000 R* for 9-*cis* retinal, which is blue-shifted in its absorption and has lower quantum efficiency (Hurley et al., 1977; Kolesnikov et al., 2018; Sekharan and Morokuma, 2011).

We analyzed luminance contrast encoding of ganglion cells with linear-nonlinear (LN) models constructed from responses to Gaussian white noise stimuli (Chichilnisky, 2001; Pearson and Kerschensteiner, 2015). In these stimuli, the display was divided into vertical bars (width: 50 μ m, height: 1.7 mm). The intensity of each bar was chosen at random every 33 ms (refresh rate: 30 Hz) from a Gaussian distribution (RMS contrast: 40%) for 30 min. At 50 s intervals, a 10 s segment of white noise was repeated. Spatiotemporal receptive fields (i.e., the linear component of the LN models) were mapped by computing spike-triggered stimulus averages (STA) from a non-repeating part of the Gaussian white noise. A separate non-repeating part of the stimulus was convolved with the STA to calculate a vector of generator signals and estimate contrast-response functions. At each time point, the generator signal describes the match between the spatiotemporal receptive field and the preceding stimulus (i.e., the effective stimulus contrast). The dependence of the firing rate on the generator signal was fit with a sigmoidal function (i.e., the nonlinear component of the LN models):

$$r(g) = \alpha C(\beta g - \gamma) + \delta$$

where $r(g)$ is the firing rate as a function of the generator signal, C is the cumulative normal distribution function, and α , β , γ , and δ are free parameters. LN model performance was tested by comparing its predictions to the observed responses during the repeated white-noise segment. Only cells whose LN models explained > 35% of the response variance were included in the subsequent analysis. We confirmed that variation of this threshold from 0% (i.e., no threshold) to 50% did not affect our conclusions. To compare temporal receptive fields of different ganglion cells, we calculated the time to peak sensitivity (i.e., time to peak or TTP), the time to the subsequent zero-crossing (i.e., time to zero or TTZ), and a biphasic index (bi):

$$bi = 1 - \frac{|peak + trough|}{|peak| + |trough|}$$

where *peak* and *trough* refer to the maximum and minimum of the temporal filter, respectively. To estimate receptive field sizes, we calculated the variance of different bars across the time of the STA and fit a Gaussian function to the result. The receptive field size was defined as one standard deviation of the Gaussian. To compare contrast-response functions (Chichilnisky and Kalmar, 2002; Pearson and Kerschensteiner, 2015; Ravi et al., 2018), we computed their nonlinearity as the logarithm of the ratio of the slope at the response maximum to the slope of the response at generator signal = 0, their gain as the logarithm of the slope at generator signal = 0, and their threshold as a percentage of the range of effective stimulus contrasts (–100% to 100%) at which the response reaches 10% of its maximum.

We also tested ganglion cell responses to full-field contrast steps. At 2 s intervals, 0.5 s steps of varying intensity (*I*) were presented from a gray background (*I_b*). All steps were presented 20 times in pseudorandom order. The Michelson contrast of each step was calculated as:

$$C = \frac{I - I_b}{I + I_b}$$

Ganglion cell responses were measured as the difference in the average firing rate in a 300-ms window after the step onset (i.e., post-step) and the average firing rate in a 300-ms window before the step onset (i.e., pre-step). In addition, we calculated the Poisson probability (*P*) of the spike counts (*N*) in both windows according to:

$$P = \frac{e^{-rT} \times (rT)^N}{N!}$$

where *r* is the average firing rate of the cell and *T* the duration of the pre- and post-step time window. We then used a two-interval forced-choice paradigm to determine contrast thresholds (Murphy and Rieke, 2011; Pearson and Kerschensteiner, 2015). When the Poisson probability of the post-step spike count was lower than that of the pre-step spike count, the step was recorded as detected. Weibull cumulative distribution functions were then fit to the contrast dependence of step detection separately for negative and positive contrasts and thresholds defined as the lowest absolute contrast levels at which detection probability reached 75%.

To explore direction preferences of ganglion cell motion responses, we presented drifting full-field square-wave gratings of varying spatial and temporal frequencies (spatial frequency: 0.25, 0.5, 1.25 cycles / °; temporal frequency: 1, 5, 10, 20 cycles / s) moving in eight pseudorandomly chosen directions at 45° intervals). In the pseudorandom sequence, each stimulus was repeated four times, and each repeat lasted 5 s. To measure direction and orientation preference, the average firing rates of a neuron to each drift direction were computed, and the average firing rate in response to interleaved uniform gray stimuli of the same mean luminance subtracted. Direction selectivity indices (*DSI*) were then calculated based on the circular variance of the response (*r*) as follows:

$$DSI = \left| \frac{\sum r(\theta)e^{i\theta}}{\sum r(\theta)} \right|$$

where *θ* indicates the direction of motion

Functional Classification of Ganglion Cells

Ganglion cells were classified based on their responses to the Gaussian white noise bar stimuli. First, ON-OFF responsive cells were identified by their U-shaped static nonlinearities (Figure S1). ON-OFF ganglion cells were not further characterized in this study, but their identification confirmed by responses to full-field light steps (data not shown). Among the remaining cells, four functional types were abundant and easily separated by their temporal receptive fields (or temporal filters). In principal component analyses (i.e., a linear dimensionality reduction approach), the first principal component of the temporal filters separated ON and OFF cells. Scatterplots of the first two principal components revealed two clusters of OFF cells, while scatterplots of the first principal component, and a monophasic index ($|(peak - trough)/(peak + trough)|$) separated two clusters of ON cells. Together these four cell types accounted for ~80% (336/424) of the recorded light-responsive cells in our study. A nonlinear dimensionality reduction approach (i.e., tSNE) (van der Maaten and Hinton, 2008) separated clusters of the same four functional cell types (data not shown). The same four cell types were reliably identified in all recordings (Figure S1). Analyses of spatial receptive fields and contrast-response functions, which were not part of the classification, revealed additional differences between cell types and consistent properties, supporting our classification. Based on the receptive field sizes and temporal dynamics, we grouped the four cell types into two mirror populations. We refer to them as ON and OFF midget and ON and OFF parasol, because of the correspondence in their spatiotemporal receptive fields to the dominant cell types in the macaque retina (Chichilnisky and Kalmar, 2002; Croner and Kaplan, 1995; Sinha et al., 2017), and because of the match in their receptive field sizes to dendritic field sizes of ON and OFF midget and ON and OFF parasol cells reported for the human retina (Dacey, 1993; Dacey and Petersen, 1992; Masri et al., 2019a). Finally, the sustained and transient responses of midget and parasol ganglion cells, respectively, to full-field contrast steps (Figure S5) and the lack of directional tuning in their responses to drifting grating stimuli (Figure S4) match properties of midget and parasol cells in macaques (Manookin et al., 2018).

Power Spectrum Analysis of Naturalistic Movies

From YouTube, we selected 100 20 s clips from 10 movies recorded with a 3-axis-stabilized handheld camera (DJI OSMO Pocket) at 60 frames per second (fps) with a resolution of 1920 × 1080 pixels, equivalent to 72.4 × 44.7° of the visual field. There was no overlap

between clips. All movies were recorded walking through natural environments (e.g., forest, grassland, beach, swamp, mountain trail). Before frequency decomposition, two corrections were implemented. First, we used the nonlinear relationship between the eccentricity and projection area (Drasdo and Fowler, 1974) to rescale clips to equal degrees of visual angle per pixel for each recording. Second, we added fixational eye movements. We obtained eye-movement traces from the DOVES dataset, which contains 200-Hz recordings from 29 healthy participants viewing natural scenes (Van Der Linde et al., 2009). Because our study focuses on how retinal output signals encode the environment for downstream processing, we removed saccadic eye movement during which downstream processing is suppressed (Binda and Morrone, 2018). Saccades were identified by their speed and occurred between periods of fixation. We denoted each eye movement trajectory within a period of fixation as an episode. To match naturalistic movies (60 fps), we downsampled concatenated episodes of fixational eye movements to 60 Hz. We added fixational eye movements to naturalistic movies by trimming the original movies to $22.24 \times 22.24^\circ$ fields of view centered on the movement trajectories. For frequency decomposition, we converted the resulting clips to grayscale and analyzed them by fast Fourier transformation (FFT). FFTs returned a 3D array. Similar to previous studies (Dong and Atick, 1995; Pitkow and Meister, 2012), the power was calculated by averaging all height dimensions given the frequency of the width and vice versa. The temporal frequencies were analyzed based on the movie frame rate. The final power spectrum (Figure 4) is the average across all recordings, each adjusted for its eccentricity and including fixation eye movements. Overall, the effect of these corrections was small (Agaoglu and Chung, 2020), and our conclusions did not change when either or both were abandoned.

Analysis of Fixational Eye Movements

The speed of eye movements in the DOVES dataset (Van Der Linde et al., 2009) was calculated as the change in gaze position (in $^\circ$) over time. Angular rotation (θ) was measured as the angular change in gaze directions from one movement to the next according to:

$$\theta = \arccosine \left(\frac{\begin{matrix} \rightarrow & \bullet & \rightarrow \\ m_i & & m_{i+1} \end{matrix}}{\begin{matrix} \rightarrow & \bullet & \rightarrow \\ m_i & & m_{i+1} \end{matrix}} \right)$$

where \rightarrow_{m_i} is the current gaze vector and $\rightarrow_{m_{i+1}}$ is the gaze vector of the next movement.

Power Spectrum Analysis of Receptive Fields

To account for the projection of the human eye (Drasdo and Fowler, 1974), we used a nonlinear conversion to determine receptive field sizes in degrees of visual angle based on the eccentricity of each recording. The conversion was well-fitted by a second-order polynomial (Dacey and Petersen, 1992):

$$\text{eccentricity}^\circ = 0.1 + 3.4 \cdot \text{eccentricity}_{mm} + 0.035 \cdot \text{eccentricity}_{mm}^2$$

For FFT analyses, we upsampled (10-fold) receptive fields and extended experimentally measured space and time domain filters via model fitting. For temporal filters (tf), our model consisted of the difference of two Gaussian membership functions:

$$tf = (\alpha_1 f_1(x; \sigma_1, c_1) - \alpha_2 f_2(x; \sigma_2, c_2)) + d$$

where

$$f(x; \sigma, c) = e^{-\frac{(x-c)^2}{2\sigma^2}}$$

and α is a positive scalar, and d is a constant for translation. We fit spatial filters with a standard difference-of-Gaussians model (Dacey et al., 2000). Power spectral densities were then estimated by FFT. For each cell, spatial and temporal frequency-domain filters were computed independently. We indicate the positions of frequency-domain filters in the power spectrum landscape of naturalistic movies by their centers of mass (Figure 4D).

Effective Contrast Distributions of Naturalistic Movies

To compute effective contrast distributions of naturalistic movies and analyze their alignment with neural response functions, we convolved 33 movie clips with experimentally measured spatiotemporal receptive fields of ON and OFF midget and ON and OFF parasol ganglion cells. To avoid redundancy, we spatially sampled movies with receptive fields with non-overlapping centers. After spatial convolution, signals were upsampled to 100 Hz to match the temporal resolution of receptive field maps. After temporal convolution, signal distributions were normalized by centering on their mean, dividing by their standard deviation, and multiplying by the experimental stimulus contrast (0.4 or 40%). Signals convolved by OFF cells were multiplied by -1 to retain the opposing signs of ON and OFF contrasts.

In our subsequent modeling, we used the experimentally determined nonlinear response functions from our LN models of ON and OFF midget and ON and OFF parasol ganglion cells. We fixed all parameters except the x axis (i.e., contrast) offsets. Both cell types in a paramorphic pair were shifted in unison to retain constant overlap. We specify shifts by the position of the intersection of ON and OFF response functions relative to contrast = 0.

Energy Consumption Analysis

To estimate the spike-related energy consumption (e_{con}) of ON and OFF midget and ON and OFF parasol ganglion cells, we computed the dot products of the effective contrast distributions ($p(g)$) of naturalistic movies and the nonlinear response functions ($r(g)$) for each channel individually:

$$e_{con} = p(g) \cdot r(g)$$

The total energy consumption of midget and parasol ganglion cells was calculated as the sum of their ON and OFF channels' expenditures.

Stimulus Coverage Analysis

The stimulus coverage of a cell was calculated as the Riemann sum of its effective contrast distribution p over the dynamic range of its response function. The dynamic range was determined by the crossing two thresholds of the underlying cumulative distribution functions: one low (t_{low}) and one high (t_{high}). t_{low} was defined by the intersection of experimentally measured ON-OFF response functions (midget: 6.09%, parasol: 5.52%). t_{high} was defined as $1 - t_{low}$. The stimulus coverage (cov) was then calculated as:

$$cov = \sum_{g=ON_{low}}^{ON_{high}} p_{ON}(g) + \sum_{g=OFF_{low}}^{OFF_{high}} p_{OFF}(g)$$

where, ON_{low} , ON_{high} , OFF_{low} , and OFF_{high} denote the contrast at the respective threshold crossing of ON and OFF ganglion cell types.

Mutual Information Analysis

We estimated the mutual information between stimuli and a system of ON and OFF encoders (I_{sys}) according to:

$$I_{sys} = I(S, R_{ON}) + I(S, R_{OFF})$$

where, S , the stimulus is the luminance contrast fluctuation over time in a shared receptive-field-sized region of a naturalistic movie clip. R_{ON} and R_{OFF} denote the firing rates of ON and OFF cells, respectively, which were derived by convolving the shared stimulus separately with ON and OFF temporal filters, adding noise estimated from the experimental data, and passing the resulting signal through the experimentally determined nonlinear response functions. Mutual information (I) is defined by the difference of marginal and joint Shannon entropies (H) as (Cover and Thomas, 2012):

$$I(X, Y) = H(X) + H(Y) - H(X, Y)$$

We define R as the firing rate varying over time. To calculate mutual information between continuous variables (e.g., S and R), we adopted a KSG estimator (Kraskov et al., 2004), also known as a k th nearest-neighbor estimator, as implemented by Holmes and Nemenman (2019).

To add noise, we first estimated signal-to-noise ratios (SNR) from responses to repeated white-noise stimulus segments according to:

$$SNR = \frac{E[r_s^2]}{\sigma_n^2}$$

where, $E[r_s^2]$ and σ_n^2 are the expected value of the response squared and the variance of the noise, respectively. We then simulated the noise by sampling from a Gaussian distribution with zero mean and standard deviation σ_n from the SNR value. Signal and noise were both processed in 50-ms time bins. Variations in the SNR from 50% - 200% of its measured value did not affect the contrast offset in system of ON and OFF encoders that maximized mutual information (i.e., optimal contrast offset). This was true for midget and parasol ganglion cells.

QUANTIFICATION AND STATISTICAL ANALYSIS

We compared parameters of LN models between ON and OFF midget and ON and OFF parasol ganglion cells within experiments by Mann-Whitney U tests. In addition to p values, we specify η^2 , calculated according to:

$$\eta^2 = \frac{z^2}{(n-1)}$$

where, z indicates the value of the z -statistic from the Mann-Whitney U test and n is the number of samples, to indicate effect size.

Neuron, Volume 107

Supplemental Information

Efficient Coding by Midget and Parasol

Ganglion Cells in the Human Retina

Florentina Soto, Jen-Chun Hsiang, Rithwick Rajagopal, Kisha Piggott, George J. Harocopos, Steven M. Couch, Philip Custer, Josh L. Morgan, and Daniel Kerschensteiner

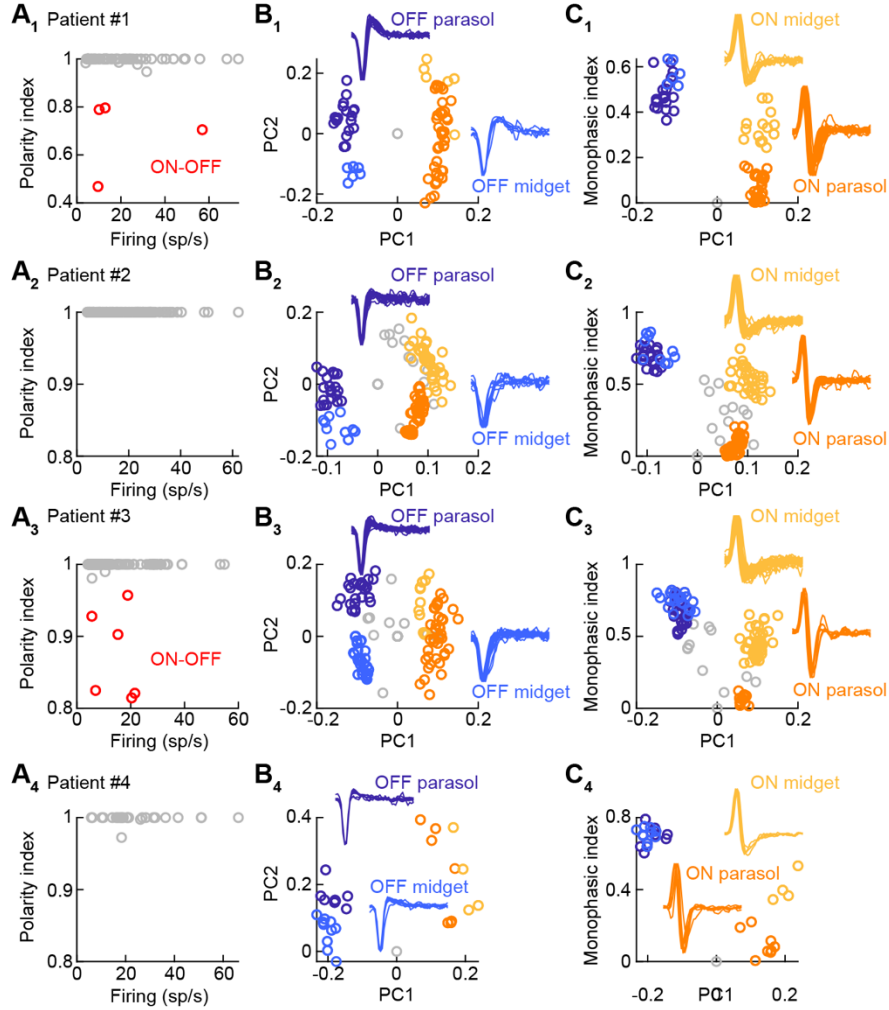


Figure S1. Functional classification of ganglion cell types. (related to Figure 1)

(A) ON-OFF ganglion cells were identified in recordings from Patient #1 (A₁), Patient #2 (A₂), Patient #3 (A₃), and Patient #4 (A₄) by a threshold in the distribution of polarity indices (pi) computed on the static nonlinearity according to $pi = (r_{high} - r_{low}) / (r_{high} + r_{low})$, where r_{high} is the difference between the firing rate at the generator signal maximum and at zero and r_{low} is the difference between the firing rate at the generator signal minimum and at zero. Negative r_{low} values were set to zero. (B) Separate clusters of OFF midget and OFF parasol ganglion cells were identified by principal component analysis of temporal receptive fields in recordings from Patient #1 (B₁), Patient #2 (B₂), Patient #3 (B₃), and Patient #4 (B₄). The boundaries between clusters were defined manually. (C) ON midget and ON parasol ganglion cells formed separate clusters in scatter plots of a monophasic index (mi) defined as, $mi = (STA_{max} - STA_{min}) / (STA_{max} + STA_{min})$, where STA_{min} and STA_{max} refer to the minimum and maximum of the temporal spike-triggered stimulus average waveform, and the first principal component of

temporal receptive fields in recordings from Patient #1 (C_1), Patient #2 (C_2), Patient #3 (C_3), and Patient #4 (C_4). The boundaries between clusters were defined manually.

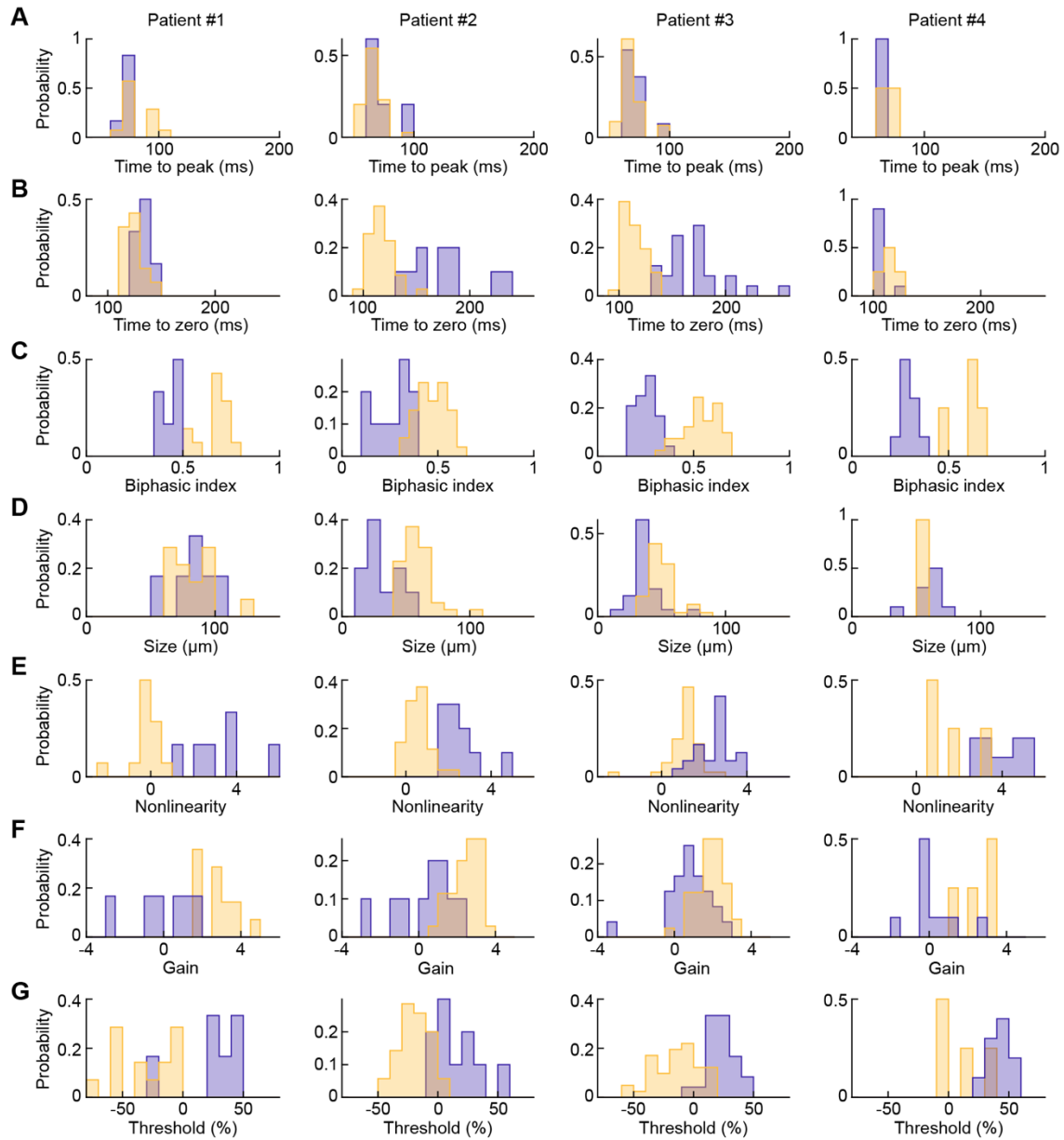


Figure S2. Light response parameters of ON and OFF midget ganglion cells. (related to Figure 2)

(A to G) Distributions ON vs. OFF midget ganglion cells from each patient comparing time to peak (A, #1 $p = 0.12$, #2 $p = 0.11$, #3 $p = 0.11$, #4 = 0.13), time to zero crossing (B, #1 $p = 0.046$, #2 $p = 2.2 \times 10^{-6}$, #3 $p = 2.3 \times 10^{-11}$, #4 $p = 0.08$), biphasic index (C, #1 $p = 6.2 \times 10^{-4}$, #2 $p = 3.2 \times 10^{-6}$, #3 $p = 2.9 \times 10^{-11}$, #4 $p = 0.002$) of the temporal receptive field, size (D, #1 $p = 0.90$, #2 $p = 1.3 \times 10^{-5}$, #3 $p = 4.4 \times 10^{-7}$, #4 $p = 0.64$) of the spatial receptive field, and nonlinearity (E, #1 $p = 6.2 \times 10^{-4}$, #2 $p = 4.2 \times 10^{-6}$, #3 $p = 8.2 \times 10^{-8}$, #4 $p = 0.008$), gain (F, #1 $p = 6.2 \times 10^{-4}$, #2 $p = 8.0 \times 10^{-5}$, #3 $p = 1.1 \times 10^{-4}$, #4 $p = 0.008$), and (G, #1 $p = 0.0044$, #2 $p = 8.1 \times 10^{-6}$, #3 $p = 8.4 \times 10^{-10}$, #4 $p = 0.008$) threshold of the effective-contrast-response function.

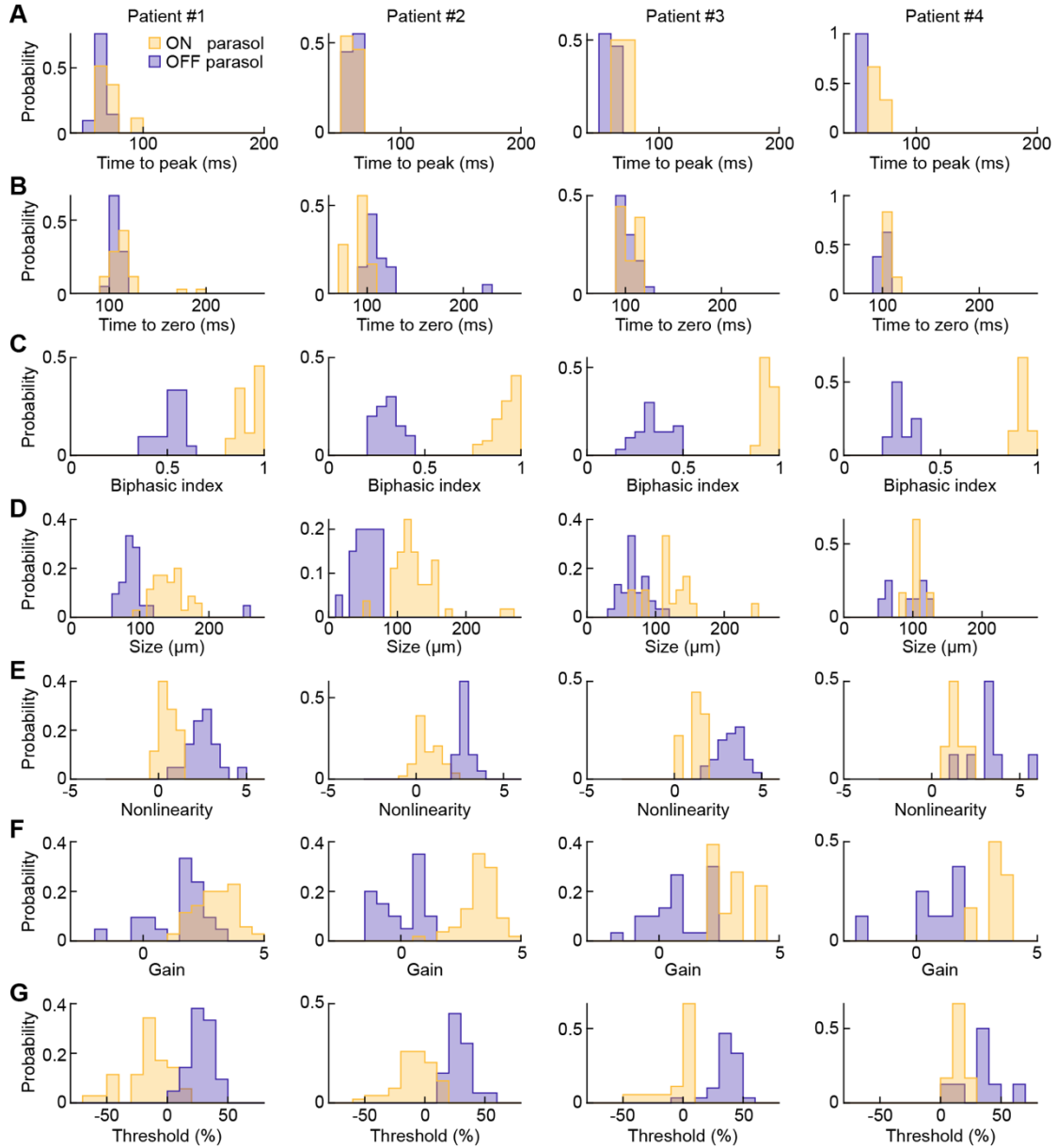


Figure S3. Light response parameters of ON and OFF parasol ganglion cells. (related to Figure 3)

(A to G) Distributions ON vs. OFF parasol ganglion cells from each patient comparing time to peak (A, #1 $p = 0.0035$, #2 $p = 0.51$, #3 $p = 1.8 \times 10^{-6}$, #4 $p = 7.0 \times 10^{-4}$), time to zero crossing (B, #1 $p = 0.046$, #2 $p = 3.5 \times 10^{-8}$, #3 $p = 0.44$, #4 $p = 0.17$), biphasic index (C, #1 $p = 5.3 \times 10^{-4}$, #2 $p = 5.1 \times 10^{-11}$, #3 $p = 9.5 \times 10^{-9}$, #4 $p = 6.6 \times 10^{-4}$) of the temporal receptive field, size (D, #1 $p = 2.6 \times 10^{-8}$, #2 $p = 2.8 \times 10^{-10}$, #3 $p = 1.3 \times 10^{-6}$, #4 $p = 0.75$) of the spatial receptive field, and nonlinearity (E, #1 $p = 1.9 \times 10^{-9}$, #2 $p = 5.2 \times 10^{-11}$, #3 $p = 2.3 \times 10^{-8}$, #4 $p = 0.0027$), gain (F, #1 $p = 3.0 \times 10^{-6}$, #2 $p = 8.4 \times 10^{-11}$, #3 $p = 2.7 \times 10^{-6}$, #4 $p = 6.6 \times 10^{-4}$), and (G, #1 $p = 1.2 \times 10^{-9}$, #2 $p = 5.2 \times 10^{-11}$, #3 $p = 4.7 \times 10^{-8}$, #4 $p = 0.02$) threshold of the effective-contrast-response function.

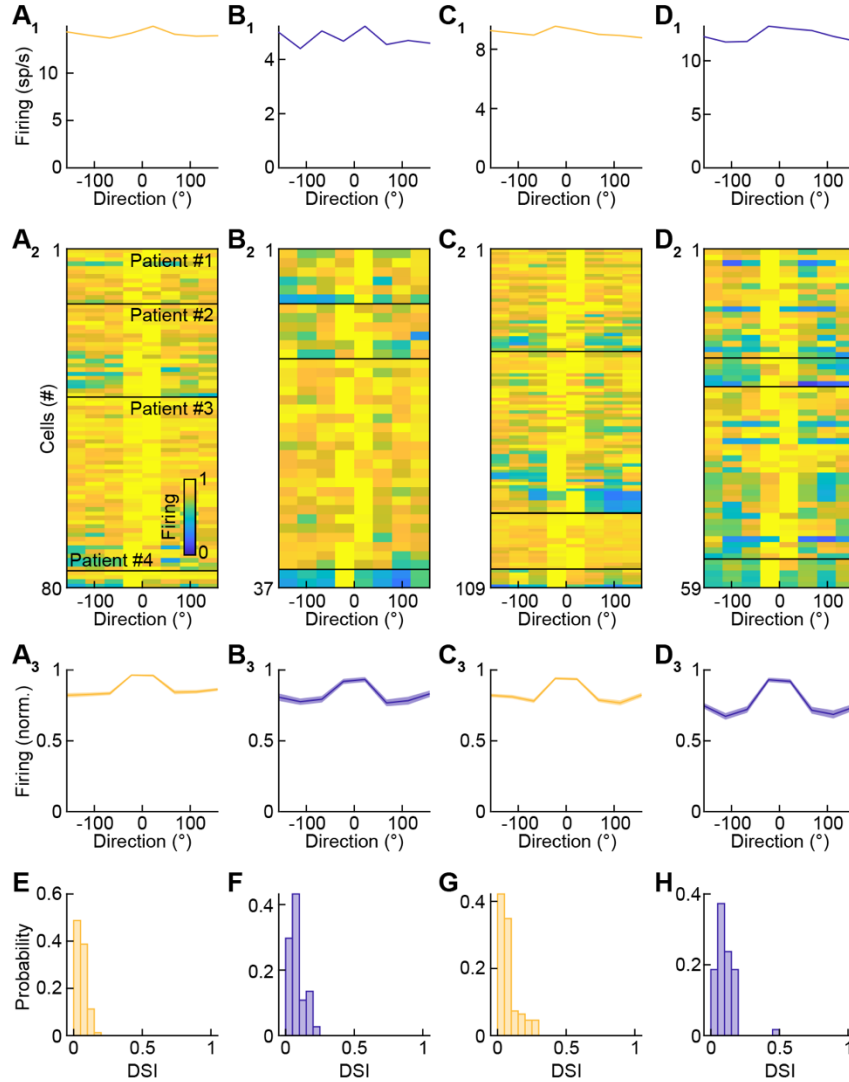


Figure S4. Midget and parasol ganglion cells are not direction selective. (related to Figure 3)

(A to D) Firing rate responses of individual (X_1), all (X_2), and the average (\pm SEM) of all (X_3) ON midget (A), OFF midget (B), ON parasol (C), and OFF parasol (D) ganglion cells to gratings drifting in different directions. All responses were centered on the direction eliciting the maximal responses and its highest-response neighbor. (E to H) Distributions of direction selectivity indices (DSI, see STAR Methods) for ON midget (E), OFF midget (F), ON parasol (G), and OFF parasol (H) ganglion cells.

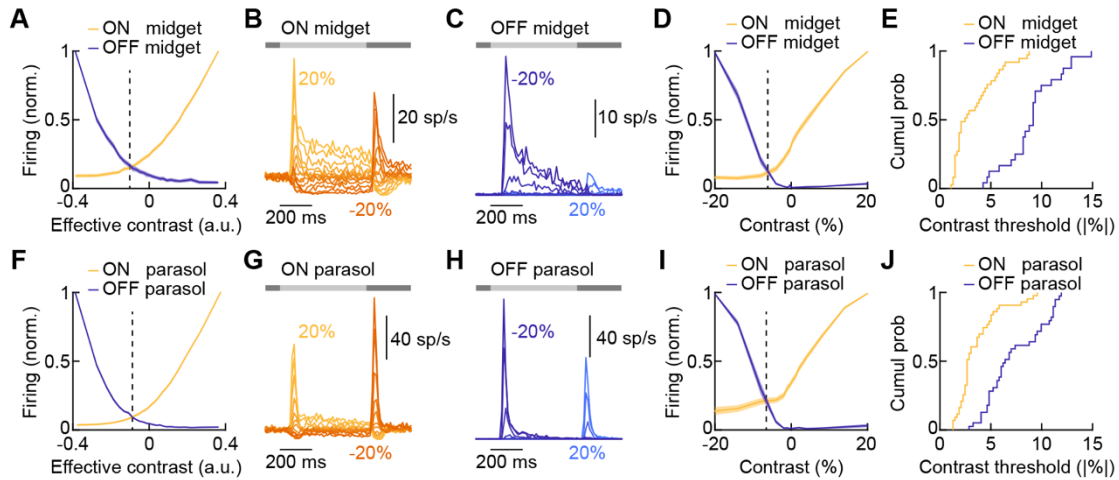


Figure S5. Asymmetric contrast-response functions of ON and OFF cells. (related to Figure 4)

(A and F) Lines (shaded areas) indicate the mean (\pm SEM) contrast-response functions of ON and OFF midget (A) and ON and OFF parasol ganglion cells (F) from white noise stimulation. Effective contrast was calculated by the convolution of the stimulus with the spatiotemporal receptive fields (see STAR Methods) and was multiplied by -1 for OFF cells. Dashed lines indicate the crossing of ON and OFF contrast-response functions. (B, C, G, and H) Representative spike responses from ON midget (B), OFF midget (C), ON parasol (G), and OFF parasol (H) ganglion cells to full-field steps of varying contrast (i.e., Michelson contrast). (D and I) Lines (shaded areas) indicate the mean (\pm SEM) contrast-response functions of ON and OFF midget (D) and ON and OFF parasol (I) ganglion cells from stimulation with full-field steps. Dashed lines mark the crossing of ON and OFF contrast-response functions. (E and J) Cumulative probability distributions of contrast thresholds of ON and OFF midget (E) and ON and OFF parasol ganglion cells. Contrast threshold was measured using a two-interval forced-choice procedure (see STAR Methods) (Murphy and Rieke, 2011; Pearson and Kerschensteiner, 2015).